Contrib Mineral Petrol (2015) 169:59
DOI 10.1007/s00410-015-1148-1

ORIGINAL PAPER

Trace-element fingerprints of chromite, magnetite and sulfides from the 3.1 Ga ultramafic–mafic rocks of the Nuggihalli greenstone belt, Western Dharwar craton (India)

Ria Mukherjee[1,2] · Sisir K. Mondal[1,4] · José M. González-Jiménez[3,5] · William L. Griffin[3] · Norman J. Pearson[3] · Suzanne Y. O'Reilly[3]

Received: 17 December 2014 / Accepted: 25 May 2015 / Published online: 24 June 2015

Abstract The 3.1 Ga Nuggihalli greenstone belt in the Western Dharwar craton is comprised of chromitite-bearing sill-like ultramafic–mafic rocks that are surrounded by metavolcanic schists (compositionally komatiitic to komatiitic basalts) and a suite of tonalite–trondhjemite–granodiorite gneissic rocks. The sill-like plutonic unit consists of a succession of serpentinite (after dunite)–peridotite–pyroxenite and gabbro with bands of titaniferous magnetite ore. The chromitite ore-bodies (length ≈30–500 m; width ≈2–15 m) are hosted by the serpentinite–peridotite unit. Unaltered chromites from massive chromitites (>80 % modal chromite) of the Byrapur and Bhaktarhalli chromite mines in the greenstone belt are characterized by high Cr# (100Cr/(Cr + Al)) of 78–86 and moderate Mg# (100 Mg/(Mg + Fe^{2+})) of 45–55. In situ trace-element analysis (LA-ICPMS) of unaltered chromites indicates that the parental magma of the chromitite ore-bodies was a komatiite lacking nickel-sulfide mineralization. In the Ga/Fe^{3+}# versus Ti/Fe^{3+}# diagram, the Byrapur chromites plot in the field of suprasubduction zone (SSZ) chromites while those from Bhaktarhalli lie in the MOR field. The above results corroborate our previous results based on major-element characteristics of the chromites, where the calculated parental melt of the Byrapur chromites was komatiitic to komatiitic basalt, and the Bhaktarhalli chromite was derived from Archean high-Mg basalt. The major-element chromite data hinted at the possibility of a SSZ environment existing in the Archean. Altered and compositionally zoned chromite grains in our study show a decrease in Ga, V, Co, Zn, Mn and enrichments of Ni and Ti in the ferritchromit rims. Trace-element heterogeneity in the altered chromites is attributed to serpentinization. The trace-element patterns of magnetite from the massive magnetite bands in the greenstone belt are similar to those from magmatic Fe–Ti–V-rich magnetite bands in layered intrusions, and magnetites from andesitic melts, suggesting that magnetite crystallized from an evolved gabbroic melt. Enrichments of Ni, Co, Te, As and Bi in disseminated millerite and niccolite occurring within chromitites, and in disseminated bravoite within magnetites, reflect element mobility during serpentinization. Monosulfide solid solution inclusions within pyroxenes (altered to actinolite) in pyroxenite, and interstitial pyrites and chalcopyrites in magnetite, retain primary characteristics except for Fe-enrichment in chalcopyrite, probably due to sub-solidus re-equilibration with magnetite. Disseminated sulfides are depleted in platinum-group elements (PGE) due to late sulfide saturation and the PGE-depleted nature of the mantle source of the sill-like ultramafic–mafic plutonic rocks in the Nuggihalli greenstone belt.

Communicated by Timothy L. Grove.

Electronic supplementary material The online version of this article (doi:10.1007/s00410-015-1148-1) contains supplementary material, which is available to authorized users.

✉ Ria Mukherjee
ria.mkrj@gmail.com

1 PGE Research Laboratory, Department of Geological Sciences, Jadavpur University, Kolkata, India

2 School of Geosciences, University of the Witwatersrand, Johannesburg 2001, South Africa

3 Australian Research Council (ARC) Centre of Excellence for Core to Crust Fluid Systems (CCFS) and GEMOC, Macquarie University, Sydney, Australia

4 Department of Earth and Planetary Sciences, American Museum of Natural History, New York, NY, USA

5 Department of Geology and Andean Geothermal Center of Excellence, Universidad de Chile, Santiago de Chile, Chile

Keywords Archean chromite · In situ trace-element · LA-ICPMS · Komatiite · Suprasubduction zone (SSZ) setting · Nuggihalli

Introduction

Chromite is an efficient petrogenetic tool (Irvine 1965; Dick and Bullen 1984; Stowe 1994; Kamenetsky et al. 2001; Ahmed and Arai 2002; Mondal et al. 2006; Rollinson 2008; Mukherjee et al. 2010), because its chemical composition is controlled by mantle melting processes that are typical of particular tectonic settings. Studying the secular changes of chromite composition in different chromitite deposits is therefore useful in understanding the evolution of Earth's upper mantle through geological time (Stowe 1994; Arai and Ahmed 2013). Chromites in massive chromitites commonly retain primary compositions in terms of major elements and can thus be used to deduce the parental melt composition and the probable tectonic setting of the chromitite deposits (e.g., Mondal et al. 2006, references therein). However, metamorphosed chromites from massive chromitites within ophiolites may be altered in terms of their minor and trace elements (e.g., González-Jiménez et al. 2013, 2014; Colás et al. 2014). The study of chromitite deposits in Archean greenstone belts helps to reveal the nature of the mantle and the tectonic processes prevalent in the Archean. The host ultramafic–mafic rocks to the chromitites in Archean greenstone belts typically are metamorphosed and hydrothermally altered and are not reliable indicators, thus making the chromites indispensable in petrogenetic studies.

In situ trace-element analysis using laser ablation ICP-MS (LA-ICPMS) has revolutionized petrogenetic studies as one can investigate the minerals of interest without interference from the surrounding phases (e.g., Dare et al. 2009, 2011, 2012; Pagé and Barnes 2009; González-Jiménez et al. 2013, 2014; Pagé et al. 2012; Colás et al. 2014). Compared to major elements in chromites, the trace elements are more sensitive to parameters like temperature and oxygen fugacity, and they therefore show larger variations during partial melting and fractional crystallization (Dare et al. 2009; González-Jiménez et al. 2013, 2014). The trace elements that enter the trivalent (Cr, Al, Fe^{3+}) octahedral site of the spinel structure, e.g., Ti, Ga, V and Co, are particularly sensitive to these processes. Thus, trace elements in chromites are useful for fingerprinting the parental melt compositions and tectonic settings of the chromite deposits. No work has been conducted so far to determine the in situ trace-element patterns of chromites in chromitites from Archean greenstone belts. In this respect, the in situ trace-element data that have been generated in this study are significant in understanding mantle conditions and tectonic processes of the Archean Earth.

Chromites from massive chromitites (>80 % modal) of the Archean Nuggihalli greenstone belt in southern India (Figs. 1, 2) have been analyzed for trace elements using LA-ICPMS. The in situ trace-element study was conducted on both unaltered chromites and in chromites with core-rim zoning, in order to compare the distribution of trace elements during primary magmatic conditions and secondary alteration. In addition to chromite, the trace elements of magnetite and sulfides (interstitial to chromite in massive chromitites and to magnetite in magnetite bands, and as inclusions in pyroxene within pyroxenite) from the Nuggihalli greenstone belt have been studied. This has been undertaken to understand their genesis and to identify the signatures of sub-solidus processes that modify their primary composition. Modification of primary magmatic compositions is expected in these minerals due to the extensive hydrothermal alteration and greenschist facies metamorphism experienced by the rocks within the greenstone belt.

Geological setting

The Nuggihalli greenstone belt is situated in the Western Dharwar craton in southern India (Fig. 1). This craton comprises several early to Mesoarchean greenstone belts (3.4–3.0 Ga; Mukherjee et al. 2012 and references therein), also known as the Sargur Group supracrustals (Swami Nath and Ramakrishnan 1981), which occur as discontinuous linear belts (30–60 km × 2–6 km) over the entire length of the craton. The Nuggihalli greenstone belt belongs to the Sargur Group, which is represented by conformable metamorphosed (low-grade greenschist to lower amphibolite facies) volcanic (e.g., komatiite to komatiitic basalts and tholeiites) and sedimentary assemblages (e.g., fuchsite-quartzites, banded-iron formations, bedded barites and kyanite-garnet-bearing quartzites and mica schists) that are surrounded by the tonalite–trondhjemite–granodiorite suite of gneisses (TTG; Fig. 1; Mukherjee et al. 2012). Sill-like chromitite-bearing layered peridotitic rocks and magnetite-bearing gabbroic rocks commonly occur within the early to Mesoarchean volcano-sedimentary supracrustals, e.g., the Nuggihalli–Holenarsipur–Krishnarajpet–Nagamangala greenstone belts (Fig. 1). The chromitite-bearing plutonic rocks in the Nuggihalli greenstone belt have been dated at 3125 ± 120 Ma by whole-rock Sm–Nd methods (Mukherjee et al. 2012).

The Nuggihalli greenstones (60 × 2 km) form a linear NNW–SSE trending belt in the Western Dharwar craton (Fig. 2). The belt is comprised of a plutonic chromitite-bearing sill-like layered ultramafic–mafic unit that is surrounded by metavolcanic schists (komatiitic to komatiitic basalts), minor metasediments and the TTG. The chromiferous ultramafic rocks occur as dismembered *en*

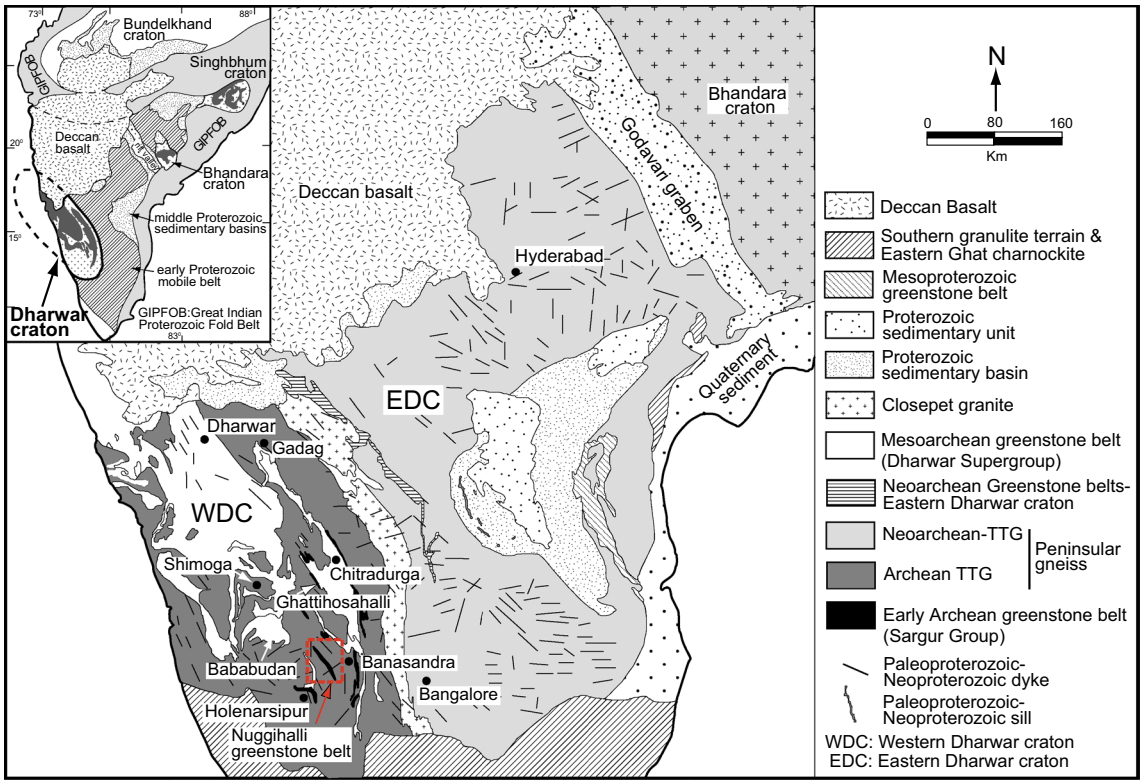

Fig. 1 Geology of the Dharwar craton showing location of the Nuggihalli greenstone belt (after Murthy 1987; cited in Devaraju et al. 2009). *Inset map* illustrates the geology of the Indian shield showing location of the Dharwar craton (compiled by Mondal et al. 2006; after Leelananadam et al. 2006; Radhakrishna and Naqvi 1986)

echelon lenticular bodies (Fig. 2). The rocks of the Nuggihalli greenstone belt are deformed and metamorphosed to low-grade greenschist facies; despite this metamorphic overprint, primary igneous textures are preserved and the protoliths can still be identified.

The sill-like layered ultramafic–mafic sequence is well exposed in the Tagdur chromite-mining district in the state of Karnataka (Fig. 2). The stratigraphic column of the rocks exposed in the greenstone belt is shown in Fig. 3. The sequence commences with a serpentinite (after dunite) and peridotite (now tremolite–talc–chlorite–actinolite schist) unit that hosts the chromitite ore-bodies, which are then stratigraphically followed by the pyroxenite and gabbro units (Fig. 3). Contacts between the chromitite body and the host serpentinite are highly sheared. The gabbro shows layering and contains two conformable bands of titaniferous–vanadiferous magnetite at its base and top (Fig. 3). The lower magnetite band (width ≈2 m) hosts disseminated pyrite, chalcopyrite and minor bravoite. The gabbro is followed by an upper ultramafic unit of chromitite-bearing serpentinite and peridotite that are further surrounded by the metavolcanic schists and TTG (Fig. 3). The contact between the metavolcanic schists and the TTG is obscured by soil cover but appears to be concordant.

Description of analyzed samples

Chromitite

The chromites analyzed by LA-ICPMS are from chromitite ore-bodies and were collected from the underground chromite mine at Byrapur and from open pits in the Byrapur, Bhaktarhalli and Tagdur mines (Fig. 2). Byrapur was the largest chromite mine that was operating with a total depth of ≈305 m (Mukherjee et al. 2010). The chromitite ore-bodies hosted within serpentinites range in length from 50 to 500 m with a width of ≈15 m, while within the peridotite unit they are approximately 30 m long with a width of 1–2 m. The chromitite ore-bodies occur as sigmoidal, lenticular, pod-shaped and folded bodies, owing to the superposed folding common in the greenstone belts (Mukherjee et al. 2014). The upper chromitite body occurring above the gabbro unit in Tagdur (Fig. 3) appears as an elongate, lenticular body (length ≈100 m; width ≈15 m; N–S trend, dipping west) that is more altered with a higher mode of carbonate (mainly magnesite; Appendix A—available online), compared to the lower chromitite body in Tagdur. The chromitites preserve primary igneous layering with serpentinite (after dunite) in which the contact between the

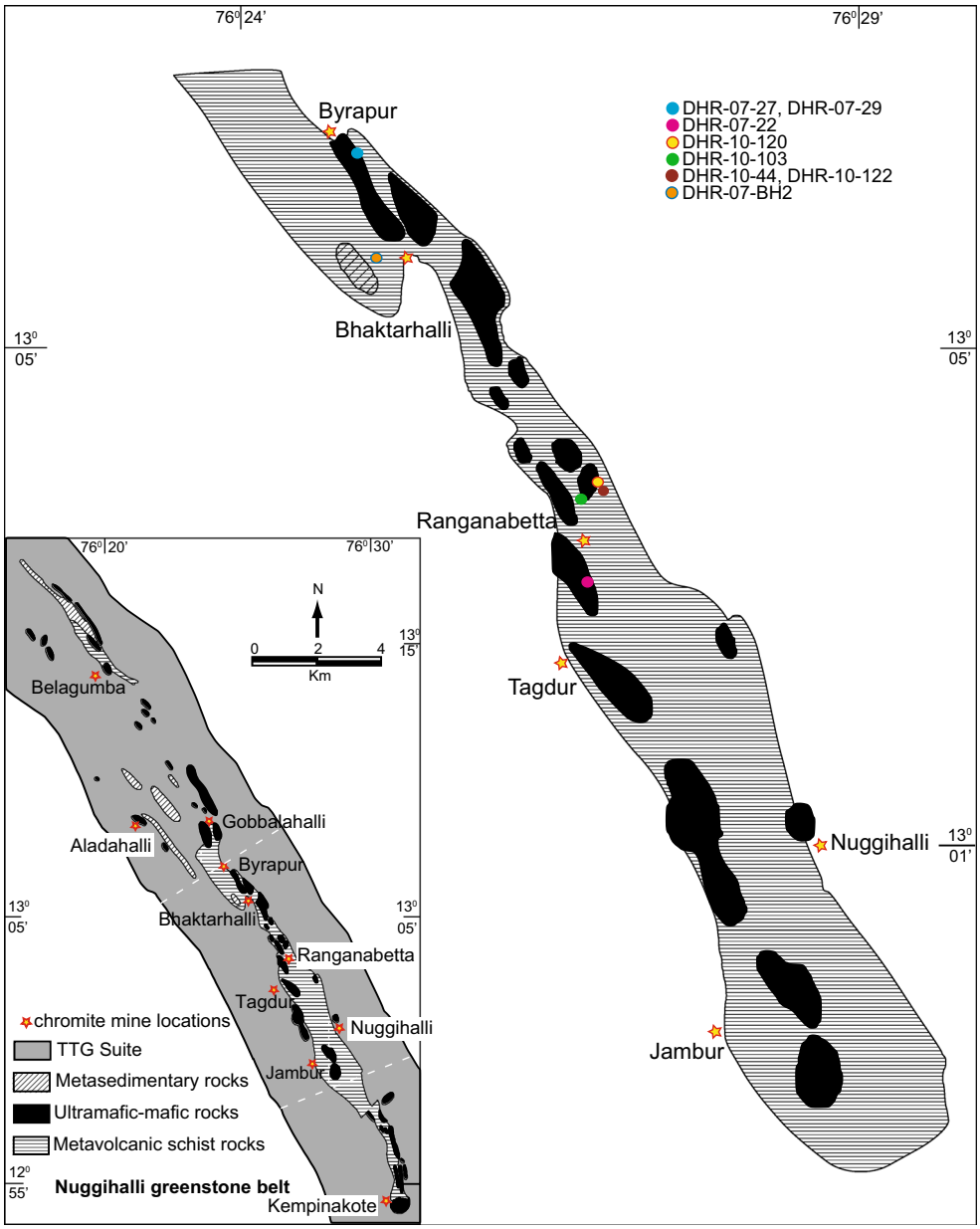

Fig. 2 Geology of the Nuggihalli greenstone belt (after Jafri et al. 1983; cited in Devaraju et al. 2009) is shown in the *left-hand corner*. The *dotted boundary marks* the area in the map that is enlarged (*right-hand side*) to show the chromite-mining districts and sample locations of this study

two rock units is gradational. The strikes of the ore-bodies are predominantly N–S and NW–SE with a nearly vertical dip (75°–80°) toward the east; at places, the strike is E–W with dip toward the north.

The chromitites studied for trace elements are mainly massive chromitites from the Byrapur and Bhaktarhalli mine (≈70–85 % modal chromite), and silicate-rich chromitites (≈50 % modal chromite) from the Tagdur chromite mine. The Byrapur chromites are coarse-grained, euhedral, polygonal and less deformed (Fig. 4a). The chromitite contains relict olivine ($Fo_{96–98}$; Mukherjee et al. 2010) and orthopyroxene [Mg#: (100 Mg/(Mg + Fe^{2+})) = 97–99; Mukherjee et al. 2010] grains that occur both interstitially to the chromite grains and as inclusions within chromite. These chromitites are relatively fresh and unaltered compared to the chromitites in Tagdur. The massive chromitite in Bhaktarhalli is comprised of euhedral, polygonal chromite grains with microfractures. The chromite grains are extremely coarse (>1 mm), and there is hardly any interstitial material between the grains (Fig. 4b). The Byrapur

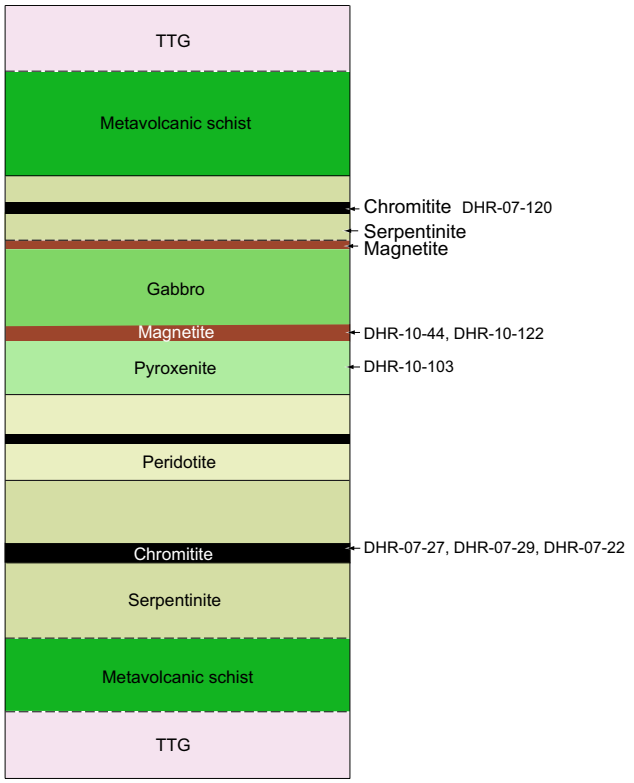

Fig. 3 Lithostratigraphy of the plutonic sill-like ultramafic–mafic complex with the surrounding metavolcanic schists and TTG in the Nuggihalli greenstone belt (Mukherjee et al. 2014). Samples collected from each lithounit are indicated in the figure with detailed description in Appendix A (available online)

chromitites contain disseminated interstitial sulfide minerals (20–50 μm) represented by millerite and minor niccolite (Fig. 4c). Inclusions (0.5–1.0 μm) of composite assemblages of millerite and niccolite are common within the Bhaktarhalli chromite grains (Fig. 4d).

The modes of altered silicate minerals vary considerably (≈10–50 %) in the massive chromitites at Tagdur. The chromite grains in these massive chromitites are highly altered. In reflected light and in scanning electron microscope (SEM), the altered grains exhibit strong compositional zoning with a darker core that is surrounded by an outer highly reflectant rim of ferritchromit (Fig. 4e, f). Ferritchromit often occurs as small irregular patches or along fractures within chromite grains (Fig. 4f). Locally, the ferritchromit is surrounded by either a discontinuous or continuous rim of magnetite (Mukherjee et al. 2010). Magnetite is rare compared to ferritchromit but may also occur along fractures within the chromite grains (Mukherjee et al. 2010). The smaller broken chromite grains in the silicate-rich chromitites from Tagdur are completely oxidized to ferritchromit and magnetite, while the larger cumulus grains are less altered (Fig. 4e, f). Lamellar Cr-bearing chlorite is a common associate in the alteration assemblage that occurs along veins and grain boundaries of chromite. Magnesite occurs as micro-veins within chromite, and at places, these veins transgress the antigorite.

Pyroxenite

Pyroxenite is poorly exposed at Tagdur but has been reported from other localities in the belt such as Byrapur (e.g., Radhakrishna 1957). At Tagdur, the pyroxenite is present between the chromitite-bearing serpentinite and peridotite and the magnetite-bearing gabbro units (Fig. 3). It shares sheared and conformable contacts with the lower magnetite ore band. The rock is composed of chlorite, actinolite, quartz, and minor tremolite and hornblende (Fig. 4g), and lacks an overall fabric as all grains are randomly oriented. Common accessory phases include ilmenite (Fig. 4h). Actinolite occurs as long prismatic blades (Fig. 4g). A few coarse grains of orthopyroxene (hypersthene) are also present (Fig. 4g), and chlorite laths cut across actinolite and hypersthene grains. Small (2–15 μm) subhedral grains of sulfide occur as inclusions within the actinolite grains commonly in multiples and sometimes in isolation (Fig. 4i). These sulfides have been analyzed for trace elements.

Magnetite ores

The ores of magnetite are coarse-grained and have experienced extensive martitization (oxidation to hematite) (Fig. 4j) probably during the hydrothermal alteration events that affected the entire Nuggihalli greenstone belt. However, remnant patches of magnetite are still preserved in places. The martitized magnetites show exsolution of ilmenite along well-defined crystallographic planes, in a trellis texture (e.g., Haggerty 1991; Fig. 4j). Ilmenite also occurs as blebs within magnetite or at the oxide–silicate (chlorite) interfaces (Fig. 4j–l). This type of exsolution is termed granule oxy-exsolution, where ilmenite tends to migrate to magnetite grain boundaries at high temperatures, forming blebs (Buddington and Lindsley 1964; Haggerty 1991). In contrast, at lower temperatures ilmenite is confined within the host magnetite grain as lamellae due to the slower diffusion rates (Buddington and Lindsley 1964).

The rock is deformed, which has resulted in sintering of the oxide grains along with shearing of the interstitial chlorite. Coarse- to medium-grained subhedral chalcopyrite and pyrite occur within the oxide grains and also at oxide–chlorite and oxide–oxide interfaces (Fig. 4k–l). Bravoite ($FeNiS_2$) replaces pyrite, with which it shares curved and matching boundaries; it also occurs as isolated grains within the chlorite matrix (Fig. 4k).

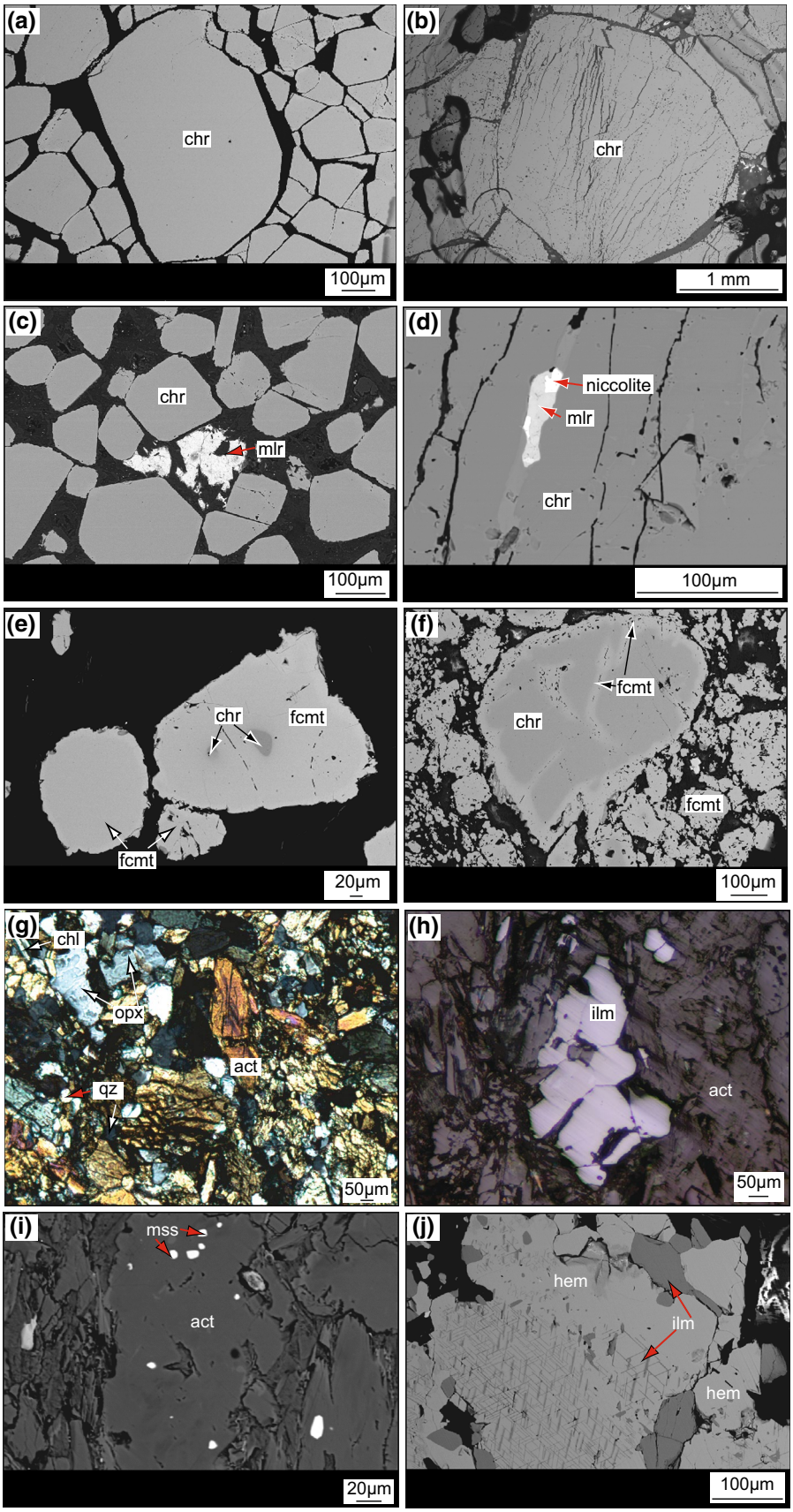

Fig. 4 BSE images of chromites in chromitites from the Nuggihalli greenstone belt **a** polygonal coarse-grained euhedral unaltered chromite (chr) from massive chromitite; sample DHR-07-29, **b** extremely coarse-grained euhedral unaltered chromite (chr) from massive chromitite; sample DHR-07-BH2, **c** interstitial disseminated millerite (mlr) in massive chromitite; sample DHR-07-27, **d** composite grain of millerite (mlr) and niccolite as inclusion within chromite from massive chromitite; sample DHR-07-BH2, **e** altered subhedral chromites (chr) from silicate-rich chromitite showing irregular grain boundaries and compositional zoning (larger grain). Remnant chromite core is replaced by high-reflectant ferritchromit (fcmt) rim; adjacent unzoned grains are homogeneously altered to ferritchromit; sample DHR-07-22, **f** irregular ferritchromit (fcmt) occurrence along fractures in altered chromite (chr); surrounding smaller chromites are homogeneously altered to ferritchromit; sample DHR-10-120, **g** photomicrograph in transmitted light (under crossed polars) showing actinolite (act), chlorite (chl), remnant orthopyroxene (opx) and quartz (qz) grains in the pyroxenite; sample DHR-07-26, **h** ilmenite grains (ilm) within the pyroxenite; in reflected light, sample DHR-10-103, **i** BSE image of multiple inclusions of small, rounded to subhedral grains of monosulfide solid solution (MSS) within actinolite grains in the pyroxenite; sample DHR-10-103, **j** BSE image of magnetite grain showing oxidation to hematite (hem) and exhibiting ilmenite exsolution (trellis texture); sample DHR-10-122, **k** photomicrograph in reflected light of interstitial disseminated sulfide grains of chalcopyrite (ccp), pyrite (py) and bravoite in the interstitial spaces within the magnetite; sample DHR-10-122, **l** photomicrograph in reflected light of disseminated sulfide grains of pyrite (py) and chalcopyrite (ccp) within the magnetite; sample DHR-10-44. Mineral abbreviations are from Whitney and Evans (2010)

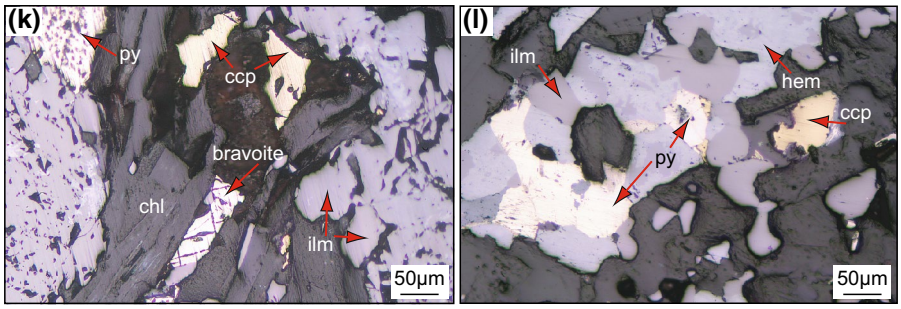

Fig. 4 continued

Analytical methods

The in situ trace-element concentrations in chromite, magnetite and sulfides were measured by LA-ICPMS in the ARC Centre of Excellence for Core to Crust Fluid Systems (CCFS) and GEMOC National Key Centre in Macquarie University, Sydney (Australia). The compositions of these minerals were first obtained using EPMA (Appendix B, D, E—available online), for internal standardization of the data acquired by LA-ICPMS. The major-element analyses were performed on the marked and mapped polished sections using a Cameca SX100 electron microprobe in the Geochemical Analysis Unit, GEMOC, Macquarie University (Sydney, Australia). The instrument was operated at 15 kV acceleration voltage, 20 nA sample current and 10 s measurement time (peak) for Ca, Cr, Fe, K, Mn, Na, Ni, Ti, V, Zn, whereas 20 s measurement time was used for Mg and Si, and 30 s for Al. Standards used were a combination of natural and synthetic minerals and pure metals. Matrix corrections followed the method by Pouchou and Pichoir (1984).

The laser ablation (LA) ICP-MS system in the Geochemical Analysis Unit at GEMOC consists of a New Wave UP 213 laser system connected to an Agilent 7700cs ICP-MS. Chromite and magnetite grains were analyzed for the following masses: ^{27}Al, ^{47}Ti, ^{51}V, ^{53}Cr, ^{55}Mn, ^{57}Fe, ^{59}Co, ^{60}Ni, ^{66}Zn and ^{71}Ga. The beam size ranged from 20 to 55 μm. Each analysis was conducted over 180 s (60 s for the gas blank and 120 s on the chromite and magnetite) using a 5-Hz frequency and 4.16 mJ/pulse power. The instrument was calibrated against an external standard, the NIST 610 silicate glass (National Institute of Standards and Technology, Gaithersburg, USA (Norman et al. 1996)), and the in-house chromite standard LCR-1 (Lace mine, South Africa). The latter was analyzed as an unknown to assess the accuracy and precision of the analyses of Al, Ti, V, Co and Ni. The reference material BCR2 (Basalt, Columbia River; prepared as a glass) was also analyzed as an unknown to check the accuracy and precision. The NIST standard was checked for any drift during each analytical run. The certified values of the standards, and the average analysis of the in-house chromite standard against NIST 610 for different runs during the laser ablation process, are tabulated in Appendix C (available online). All data were processed using the GLITTER software (Griffin et al. 2008) and are presented in Tables 1, 2. The NIST 610 glass was used to determine trace-element concentrations other than PGE in chromite, using EMP values for Al as the internal standard.

For sulfides, the in-house nickel–sulfide standard PGE-A (Alard et al. 2000) was used, with S (from EMP) as the internal standard. The beam size during analysis ranged from 30 to 40 μm. The PGE-A standard was also analyzed as an unknown to assess possible spectral interferences. The average values of PGE-A for different runs during the laser ablation analysis are tabulated in Appendix F (available online). The data were processed using GLITTER and are presented in Table 3.

Results

Chromite

The compositions of chromites from the Nuggihalli greenstone belt have been characterized previously using electron microprobe analysis (Mukherjee et al. 2010). Additional electron microprobe analyses were conducted on the laser-ablated chromites in this study as a pre-requisite for data acquisition by LA-ICPMS. The compositional field of chromites from our previous study (Mukherjee et al. 2010) and the newly acquired data from this study are presented in Fig. 5a, and the compositional data for chromite cores are plotted in Fig. 5b. The unaltered chromites from Byrapur and Bhaktarhalli have high and almost constant Cr# (100Cr/(Cr + Al)) of 85–86 and moderate and variable Mg# (100 Mg/(Mg + Fe^{2+})) of 45–48 (Fig. 5; Appendix B—available online). However, compared to the Byrapur chromites, the ones from Bhaktarhalli show higher Mg# (51–55) and a lower Cr# (78–79) due to their higher concentrations of Al_2O_3 and MgO (Fig. 5; Appendix B—available online). The unaltered chromite grains follow the *chr-1* trend, which is characterized by constant and high Cr ratios and variable Mg ratios (Fig. 5a–b).

Table 1 In situ trace-element data (LA-ICPMS; ppm) for unaltered and altered chromite grains from chromitites of the Nuggihalli greenstone belt

	DHR-07-29A Core $n = 2$	DHR-07-29A Rim $n = 3$	DHR-07-27 Core $n = 2$	DHR-07-27 Rim $n = 3$	DHR-07-BH2 $n = 3$	DHR-07-22 Grain 1 Core $n = 1$	DHR-07-22 Grain 1 Rim $n = 1$
Sc	4.2 (0.1)	4.9 (0.2)	4.6 (0.2)	4.9 (0.2)	6.6 (0.2)	3.9 (0.1)	1.8 (0.1)
Ti	3116 (97)	3139 (98)	2658 (83)	2670 (84)	1795 (57)	1440 (46)	1517 (48)
V	628 (20)	637 (21)	488 (16)	491 (16)	543 (26)	853 (26)	467 (14)
Mn	2288 (72)	2310 (73)	2516 (80)	2548 (81)	2175 (81)	5355 (169)	3966 (125)
Co	244 (8)	236 (7)	223 (7)	232 (7)	201 (9)	866 (27)	350 (11)
Ni	749 (24)	939 (30)	785 (26)	731 (24)	776 (33)	432 (14)	584 (19)
Zn	693 (24)	684 (24)	706 (25)	710 (25)	422 (18)	8946 (376)	1816 (77)
Ga	25 (0.8)	25 (0.8)	21 (0.7)	22 (0.8)	25 (0.9)	26 (0.9)	5.9 (0.2)

	DHR-07-22 Grain 2 Core $n = 1$	DHR-07-22 Grain 2 Rim $n = 1$	DHR-07-22 Grain 3 Core $n = 1$	DHR-07-22 Grain 3 Rim $n = 1$	DHR-07-22 Grain 3 (adjacent grain) Core $n = 1$	DHR-07-22 Grain 3 (adjacent grain) Rim $n = 1$	DHR-07-22 Grain 4 Core $n = 1$
Sc	7.4 (0.2)	8.2 (0.3)	5.8 (0.2)	0.6 (0.02)	3.3 (0.1)	2.3 (0.1)	0.1 (0.01)
Ti	1651 (52)	6867 (217)	1680 (54)	545 (17)	2915 (93)	1946 (62)	198 (6)
V	893 (27)	2218 (68)	869 (27)	158 (5)	890 (27)	576 (18)	124 (4)
Mn	5554 (175)	19,534 (615)	5442 (173)	1292 (41)	7751 (247)	4783 (152)	843 (27)
Co	867 (27)	1695 (53)	863 (27)	113 (4)	675 (21)	411 (13)	127 (4)
Ni	571 (19)	2793 (91)	503 (17)	205 (7)	1161 (38)	744 (25)	49 (2)
Zn	8780 (368)	9721 (406)	9189 (394)	579 (25)	3561 (156)	2306 (100)	1260 (56)
Ga	31 (1)	27 (0.9)	30 (1)	1.6 (0.1)	10 (0.3)	6.6 (0.2)	1.5 (0.1)

	DHR-07-22 Grain 4 Rim 1 $n = 1$	DHR-07-22 Grain 4 Rim 2 $n = 1$	DHR-07-22 Grain 4 Rim 3 $n = 1$	DHR-10-120 grain 1 Core $n = 1$	DHR-10-120 Grain 1 Rim $n = 1$	DHR-10-120 Grain 2 Core $n = 1$	DHR-10-120 Grain 2 Rim $n = 1$
Sc	9.9 (0.4)	4.9 (0.3)	7.5 (0.3)	2.3 (0.1)	5.7 (0.2)	2.0 (0.1)	31 (1)
Ti	8929 (285)	4975 (161)	6572 (211)	1158 (38)	2167 (70)	839 (27)	7444 (245)
V	2837 (87)	1409 (43)	1828 (56)	639 (20)	471 (15)	607 (19)	1689 (52)
Mn	25,176 (803)	12,295 (394)	16,187 (520)	2062 (67)	1284 (42)	1869 (60)	5861 (189)
Co	2255 (72)	1123 (36)	1336 (43)	630 (20)	250 (8)	598 (19)	1137 (37)

Table 1 continued

	DHR-07-22 Grain 4 Rim 1 $n = 1$	DHR-07-22 Grain 4 Rim 2 $n = 1$	DHR-07-22 Grain 4 Rim 3 $n = 1$	DHR-10-120 grain 1 Core $n = 1$	DHR-10-120 Grain 1 Rim $n = 1$	DHR-10-120 Grain 2 Core $n = 1$	DHR-10-120 Grain 2 Rim $n = 1$
Ni	3584 (119)	1953 (66)	2362 (79)	137 (5)	200 (7)	114 (4)	593 (22)
Zn	13,039 (575)	5162 (233)	7028 (320)	8537 (409)	2000 (100)	8350 (390)	9028 (418)
Ga	32 (1)	17 (1)	20 (1)	12 (0.4)	13 (1)	11 (0.4)	46 (2)

In situ analysis on chromites from GEMOC and CCFS, Macquarie University, Sydney (Australia). Average values of core and rim presented for unaltered chromites within massive chromitites from Byrapur and Bhaktarhalli; $n =$ number of laser points; 1σ error denoted in brackets

Table 2 In situ trace-element data (LA-ICPMS; ppm) for magnetite, ilmenite and hematite from magnetite ore-bodies of the Nuggihalli greenstone belt

		DHR-10-44 Magnetite $n = 3$	DHR-10-44 Ilmenite $n = 2$	DHR-10-44 Hematite $n = 2$	DHR-10-122 Ilmenite $n = 2$	DHR-10-122 Hematite $n = 2$
Sc	avg	15	108	0.7	117	0.8
	1σ	(0.5)	(4)	(0.03)	(4)	(0.1)
Ti	avg	81,700	299,700	353	307,300	673
	1σ	(2590)	(9480)	(11)	(9720)	(22)
V	avg	13,237	2212	8540	2531	6638
	1σ	(456)	(81)	(288)	(90)	(220)
Cr	avg	1850	48.5	442	124	793
	1σ	(59)	(1.8)	(14)	(4)	(25)
Mn	avg	2194	7122	52.7	6121	53.2
	1σ	(73)	(247)	(1.7)	(208)	(1.8)
Co	avg	102	62.4	60.4	1821	48.5
	1σ	(4)	(2)	(1.9)	(58)	(1.6)
Ni	avg	859	37	504	1492	450
	1σ	(29)	(1.3)	(17)	(49)	(15)
Zn	avg	915	214	11.7	394	4.2
	1σ	(34)	(9)	(0.5)	(16)	(0.3)
Ga	avg	87	1.0	56	3.5	45
	1σ	(2.9)	(0.1)	(1.8)	(0.2)	(1.5)
Ge	avg	11	3.2	6.5	3.3	5.5
	1σ	(0.5)	(0.2)	(0.3)	(0.2)	(0.3)
Zr	avg	0.7	1.3	0.2	1.0	0.03
	1σ	(0.1)	(0.1)	(0.01)	(0.1)	(0.01)
Nb	avg	1.2	4.7	0.01	4.3	0.01
	1σ	(0.1)	(0.2)	(0.0)	(0.2)	(0.0)
Hf	avg	0.1	0.2	0.02	0.2	0.03
	1σ	(0.02)	(0.03)	(0.01)	(0.03)	(0.01)
Ta	avg	0.2	0.3	0.0	0.3	
	1σ	(0.01)	(0.02)	(0.0)	(0.02)	

In situ analysis on oxides from GEMOC and CCFS, Macquarie University, Sydney (Australia). $n =$ number of laser points; the 1σ error is denoted in brackets

Altered chromite grains from silicate-rich chromitites in Tagdur (both the lower and upper chromitite units; Fig. 3) show distinctly darker cores surrounded by high-reflectance rims of ferritchromit and rarely magnetite (Fig. 4e–f) (Mukherjee et al. 2010). The cores are modified and show a range of Cr# from 64 to 79 and Mg# from 8 to 15 (Fig. 5a), while the rims show lower Mg# (2–6) and higher Cr# (85–99) (Fig. 5a) and Fe^{3+}# ($100 \times Fe^{3+}/(Cr + Al + Fe^{3+})$) (23–77) (Appendix B—available online). The altered grains follow the *chr-2* trend, which is characterized by sharply increasing Cr# with moderate decrease in Mg# (Fig. 5b). The core compositions of the altered grains lie either close

Table 3 In situ trace-element data (LA-ICPMS; ppm) for sulfides from massive chromitite, magnetite and pyroxenite of the Nuggihalli greenstone belt

		DHR-10-122 ccp $n = 2$	DHR-10-122 py $n = 2$	DHR-10-122 bravoite $n = 2$	DHR-10-44 ccp $n = 2$	DHR-10-44 py $n = 3$
Co	avg	0.6	212	72,874	25	1870
	1σ	(0.1)	(3)	(7230)	(164)	(80)
Ni	avg	18	9506	206,127	334	6766
	1σ	(0.5)	(355)	(7556)	(1220)	(626)
Cu	avg	199,437	11	2477	209,211	15
	1σ	(44,285)	(2.8)	(555)	(15,485)	(99)
As	avg	0.3	3.0	6.3	0.7	81
	1σ	(0.1)	(0.3)	(0.6)	(0.2)	(3.5)
Se	avg	158	242	565	176	325
	1σ	(18)	(28)	(62)	(9)	(16)
Ru	avg		0.01	0.14	0.1	0.01
	1σ		(0.01)	(0.04)	(0.02)	(0.01)
Rh	avg	2.0	0.0	0.02	3.7	0.0
	1σ	(0.2)	(0.0)	(0.01)	(0.2)	(0.0)
Ag	avg	0.4	0.3	29	5.7	0.3
	1σ	(0.04)	(0.03)	(1.8)	(6)	(0.3)
Pd	avg	0.1	0.03		0.01	
	1σ	(0.03)	(0.02)		(0.01)	
Te	avg	1.1	0. 6	74	1.1	0.9
	1σ	(0.2)	(0.1)	(5.6)	(0.1)	(0.2)
Os	avg				0.1	
	1σ				(0.01)	
Ir	avg		0.02	0.01		0.0
	1σ		(0.01)	(0.01)		(0.0)
Pt	avg			0.01		0.01
	1σ			(0.01)		(0.0)
Au	avg		0.0	0.02	0.01	0.01
	1σ		(0.0)	(0.01)	(0.02)	(0.0)
Pb	avg	6.4	3.0	25	7.0	1.0
	1σ	(0.7)	(0.4)	(2.7)	(4.8)	(0.8)
Bi	avg	0.2	0.2	3.4	0.4	0.2
	1σ	(0.03)	(0.02)	(0.2)	(0.1)	(0.1)

		DHR-10-44 bravoite $n = 1$	DHR-07-27 mil $n = 3$	DHR-07-27 interstitial niccolite $n = 5$	DHR-07-BH2 inclusion millerite $n = 1$	DHR-10-103 mss $n = 2$
Co	avg	82,486	409	161	393	2091
	1σ	(2256)	(36)	(13)	(55)	(386)
Ni	avg	254,460	572,407	586,674	688,645	77,433
	1σ	(8101)	(19,703)	(23,811)	(21,679)	(2561)
Cu	avg	660	51	66	82	37,326
	1σ	(72)	(10)	(13)	(6.2)	(3360)
As	avg	178	1083	189,994	36,918	0.32
	1σ	(3.6)	(56)	(9620)	(1984)	(2)
Se	avg	611	55	66		79
	1σ	(27)	(7.9)	(8.6)		(30)
Ru	avg	0.3	0.7	0.8	0.7	0.6
	1σ	(0.04)	(0.1)	(0.2)	(0.2)	(0.5)
Rh	avg	0.02		0.01		0.6
	1σ	(0.0)		(0.01)		(0.2)
Ag	avg	6.4	3.5	5.4	2.2	0.9
	1σ	(1.1)	(0.4)	(0.6)	(0.3)	(0.2)
Pd	avg	0.01	0.04	0.3		0.9
	1σ	(0.01)	(0.02)	(0.1)		(0.1)

Table 3 continued

		DHR-10-44 bravoite $n = 1$	DHR-07-27 mil $n = 3$	DHR-07-27 interstitial niccolite $n = 5$	DHR-07-BH2 inclusion millerite $n = 1$	DHR-10-103 mss $n = 2$
Te	avg	73	14	15.1	8.7	20
	1σ	(2.8)	(1.1)	(1.3)	(1)	(2.5)
Os	avg		0.2	14		
	1σ		(0.1)	(2)		
Ir	avg			0.3		0.2
	1σ			(0.03)		(0.1)
Pt	avg		0.1	0.1		
	1σ		(0.04)	(0.02)		
Au	avg	0.01	0.2	0.1	0.2	0.1
	1σ	(0.0)	(0.02)	(0.01)	(0.04)	(0.04)
Pb	avg	23	28	28	167	7.2
	1σ	(2.1)	(3)	(2.3)	(19)	(1.2)
Bi	avg	4.3	3.4	3.2	3.6	7.2
	1σ	(0.3)	(0.2)	(0.3)	(0.3)	(0.7)

In situ analysis from GEMOC and CCFS, Macquarie University, Sydney (Australia). n = number of laser points; the 1σ error is denoted in brackets; ccp = chalcopyrite, py = pyrite, mil = millerite. Chalcopyrite, pyrite and bravoite occur interstitially in magnetites; interstitial and inclusions of millerite and niccolite occur within massive chromitites; and mss occurs as inclusions within pyroxenites from the Nuggihalli greenstone belt

to or within the field of chromites from komatiites that have been affected by greenschist facies metamorphism; some core compositions show very high Cr# (Fig. 5b).

In situ trace-element analysis was conducted on both unaltered chromite grains and grains that displayed distinct compositional zoning, in order to compare the distribution of trace elements across different types of chromite. Compositional variability in terms of major elements is very common in accessory chromites in primary ultramafic–mafic igneous rocks and their altered counterparts (Irvine 1965, 1967; Jackson 1969; Roeder et al. 1979). Compositional variability may arise due to (a) sub-solidus re-equilibration of the chromite with the surrounding silicate minerals or an interstitial melt (Hamlyn and Keays 1979; Scowen et al. 1991; Rollinson 1995; Mondal et al. 2006), (b) oxidation and alteration of chromites during serpentinization of the host rock and its subsequent metamorphism (Bliss and Maclean 1975; Evans and Frost 1975; Loferski and Lipin 1983; Burkhard 1993; Abzalov 1998) and (c) during retrograde metamorphism, by the action of reducing fluids, as observed in podiform chromitites from different ultramafic massifs of the central and eastern Rhodope metamorphic complex in southern Bulgaria (Gervilla et al. 2012; González-Jiménez et al. 2013; Colás et al. 2014).

The unaltered chromite grains from the Nuggihalli greenstone belt do not show any variations in trace-element concentration, which is similar to the uniformity observed for their major elements (Fig. 6a; Mukherjee et al. 2010), and therefore, they are ideal for petrogenetic study. There is a slight variation in the range of trace elements between the unaltered chromites from Byrapur and Bhaktarhalli; trace-element concentrations are slightly higher in the Byrapur chromites compared to the Bhaktarhalli chromites (Table 1). The trace-element distribution in altered chromite grains has been studied in silicate-rich chromitites hosted within serpentinites from the lower part of the plutonic ultramafic–mafic complex (e.g., DHR-07-22) and the stratigraphically higher chromitite unit (e.g., DHR-10-120) in the Tagdur mine (Fig. 3). Trace-element concentrations in altered chromites show considerable variation across single grains (Fig. 6). In the altered chromite grains from the chromitites of the lower ultramafic unit (DHR-07-22), Zn and Ga decrease from the core to the ferritchromit rim, whereas Ti and Ni show an increase in the rim (Fig. 6b–d; Table 1). Mn and V also decrease in the rim except for one grain (grain 2; DHR-07-22) that shows an increased concentration of these elements in the rim (Fig. 6c; Table 1). The drop in concentration of all trace elements and the sharp enrichment of Fe_2O_3, corresponding to Rim 1 of grain 22-R3, reflects incorporation of a thin outer magnetite rim during ablation (Fig. 6d). The cores of the altered chromite grains from sample DHR-07-22 show higher concentrations of Zn, Co, Mn and V, and a moderate enrichment of Ga compared to the unaltered chromite grains from Byrapur and Bhaktarhalli (Fig. 6b–d; Table 1). Chromite grains from sample DHR-07-22 show heterogeneous intensity of alteration and extent of ferritchromit formation, as is evident from the BSE images (Fig. 6b–d). Despite this, all the chromite grains in the sample show similar distributions (except for Mn and V) and variations in trace-element concentration during alteration to ferritchromit and magnetite.

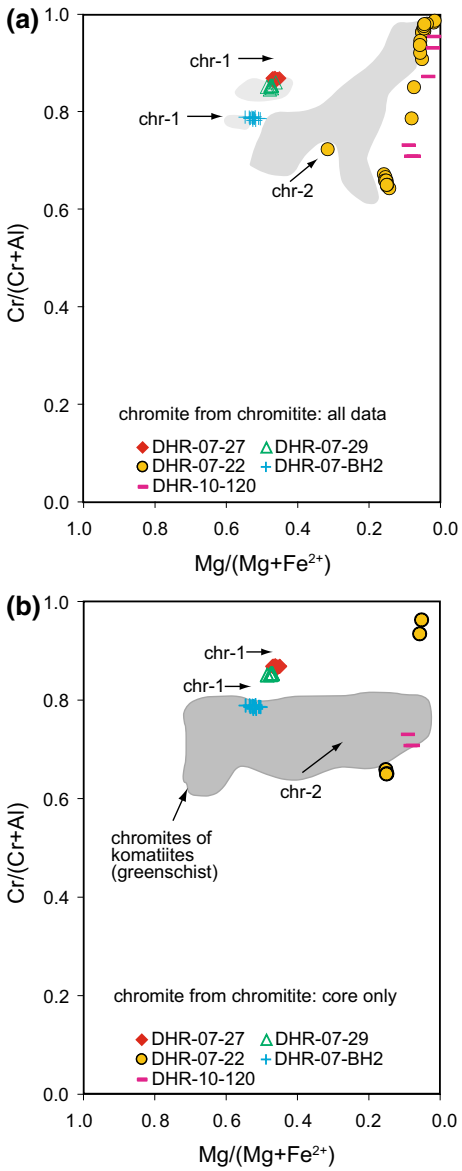

Fig. 5 Variation diagrams illustrating chromite compositions analyzed by EPMA. **a** Variation of Cr ratio against Mg ratio in chromitite; *chr-1* trend refers to decreasing Mg ratio indicating fractional crystallization in massive chromitites from Byrapur and Bhaktarhalli; *chr-2* trend illustrates alteration in chromites from silicate-rich chromitites of Tagdur where increasing Cr ratio is due to loss of Al during ferritchromit formation. The field of unaltered chromites from our previous study (Mukherjee et al. 2010) is shown in *light gray*, while the field of altered grains is shown in *dark gray*. **b** Variation of Cr ratio against Mg ratio for chromite cores in chromitite; field of altered chromite in komatiites from greenschist facies (Barnes and Roeder 2001) is shown for comparison

Altered chromite grains in massive chromitites (serpentinite-hosted) from the upper ultramafic unit in Tagdur show inter-grain variation of trace elements, where one grain (e.g., grain 1; DHR-10-120) shows a trace-element distribution pattern that is similar to the chromites from the lower ultramafic unit (Fig. 6e; Table 1), while the other (e.g., grain 2; DHR-10-120) shows a different trend (Fig. 6f; Table 1). Grain 2 exhibits an increase in concentration of all the trace elements (Zn, Mn, Ti, V, Ni and Ga) in the rim. In terms of major elements, the trend is similar, i.e., Fe_2O_3 increases from the core to the rim, while Cr_2O_3, Al_2O_3 and MgO decrease (Fig. 6e, f). The cores of the grains from the upper chromitite (DHR-10-120) show enrichment in Zn and Co, like the altered grains from the lower chromitite (DHR-07-22), while Mn and V show a range of concentrations similar to the unaltered grains from Byrapur and Bhaktarhalli (Fig. 6e, f).

Magnetite

Magnetite shows exsolution of ilmenite, which occurs as blebs within the magnetite grains or at the magnetite–silicate interface. Ilmenite also occurs as lamellae along well-defined crystallographic planes within magnetite (Fig. 4j–l). Magnetite itself has undergone extensive martitization (oxidation to hematite) (Fig. 4j), but the primary magnetite is retained in the core of a few grains. The ilmenites have TiO_2 in the range of 49–52 wt%, FeO ≈ 47–49 wt% and V_2O_3 ≈1.7–1.9 wt% (Appendix D—available online). Hematites have Fe_2O_3 in the range of 64–67 wt%, FeO ≈30–31 wt% and V_2O_3 1.2–1.4 wt% (Appendix D—available online).

The binary plots of V and Ge versus Cr concentrations in the oxide grains show a good positive correlation (Fig. 7a, b). Hematite and remnant magnetite have similar ranges of Cr, V and Ge except for one magnetite grain that has higher concentrations (Cr ≈3800 ppm; V ≈2.7 wt%; Ge ≈23 ppm; Table 2); ilmenite has lower concentrations of these elements than hematite and magnetite (Fig. 7a, b; Table 2). A similar positive correlation is observed between Ti and Cr, where magnetite shows a higher mean concentration and range in Ti relative to hematite (Fig. 7c). In contrast, ilmenite shows no covariation of Ti with Cr.

Sulfide

The major-element data for the sulfides analyzed by EPMA are presented in Appendix E—available online. Disseminated sulfides occur in the interstices of massive chromitites, and sulfides are found as inclusions within chromites from massive chromitites (millerite and niccolite) (Fig. 4c, d). Sulfide inclusions also occur within actinolite (earlier pyroxene) grains within the pyroxenite (Fig. 4i). In addition, the magnetite ores have disseminations of chalcopyrite, pyrite and bravoite in the interstitial spaces (Fig. 4k, l).

The Fe–Ni-bearing sulfides from this study are plotted in the Fe–Ni–S plot of Kullerud et al. (1969) in Fig. 8. The millerites occurring interstitially and as inclusion within chromite grains in massive chromitites (Fig. 8a) plot on the

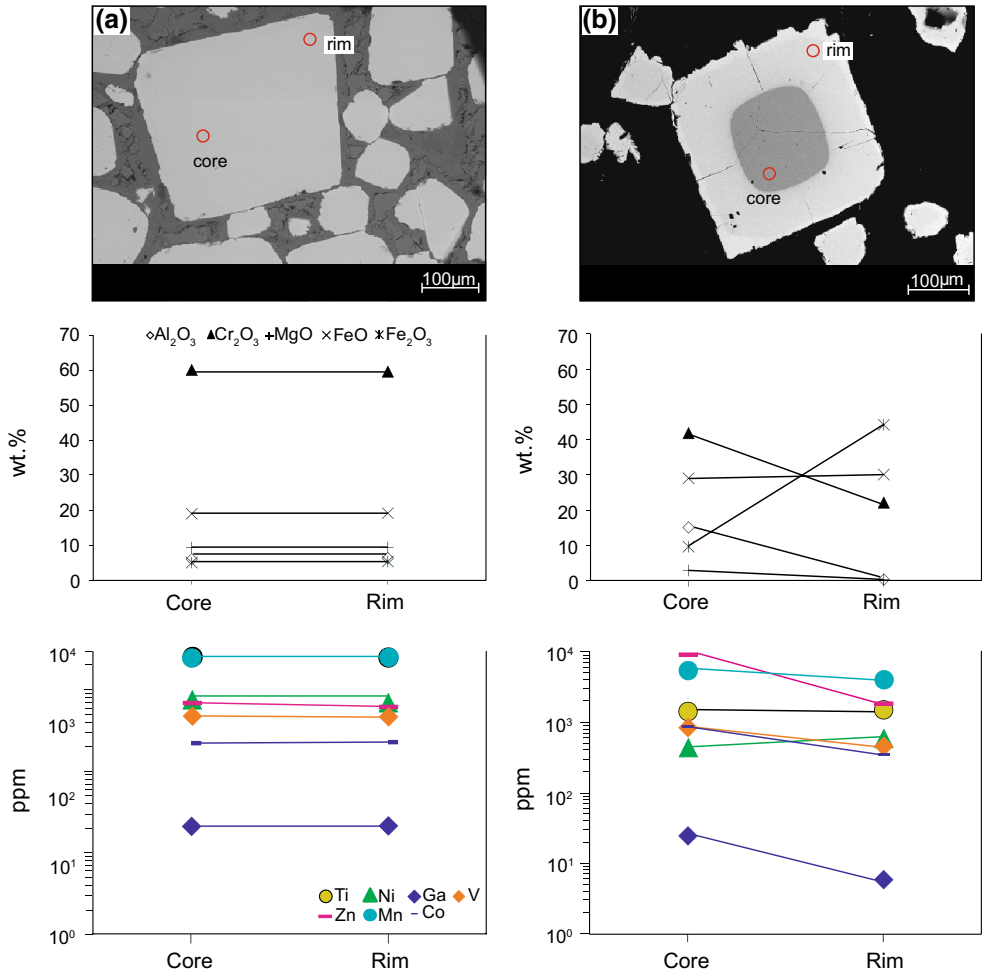

Fig. 6 Variation of major-element (analyzed by EPMA) and in situ trace-element (analyzed by LA-ICPMS) distributions in unaltered and altered chromite grains from chromitites of the Nuggihalli greenstone belt **a** unaltered chromite from massive chromitite, Byrapur; sample DHR-07-27, **b** altered chromite showing compositional zoning, silicate-rich chromitite, lower ultramafic unit, Tagdur; sample DHR-07-22 (grain 1), **c** altered and zoned chromite from silicate-rich chromitite, lower ultramafic unit, Tagdur; sample DHR-07-22 (grain 2), **d** altered chromite showing compositional zoning from silicate-rich chromitite, lower ultramafic unit, Tagdur; sample DHR-07-22 (grain 3), **e** altered and zoned chromite from silicate-rich chromitite, upper ultramafic unit, Tagdur; sample DHR-10-120 (grain 1), **f** altered chromite showing compositional zoning from silicate-rich chromitite, upper ultramafic unit, Tagdur; sample DHR-10-120 (grain 2)

Ni–S join as expected, and the pyrites interstitial to magnetites plot on the Fe–S join (Fig. 8a). Bravoite ($FeNiS_2$) plots between the pyrite and vaesite (NiS_2) joins in the Fe–Ni–S diagram (Fig. 8a). The Cu–Fe-bearing sulfides are plotted in the Cu–Fe–S diagram of Craig and Scott (1974), where the field of chalcopyrite and pyrite is illustrated (Fig. 8b). The chalcopyrites interstitial to magnetite grains do not fall in the field of typical chalcopyrite, but show slightly higher concentrations of Fe. The trace-element data for the sulfides are presented in Fig. 9. In the binary trace-element diagrams, the millerite, niccolite and bravoite show higher concentrations of Ni, Co, Te, As and Bi compared to chalcopyrite, pyrite and MSS (Fig. 9a–d; Table 3). A few of the pyrite samples show arsenic concentrations comparable to the lower range of its concentration in bravoite (Fig. 9b; Table 3). A similar observation can be made for Pb and Bi values in chalcopyrite (Fig. 9d; Table 3). Chalcopyrite and pyrite show higher concentrations of Ag and Pb (Fig. 9c; Table 3).

Discussion

Trace-element fingerprint of altered chromites: implications for chromite alteration

The compositional trend of increasing Cr# with moderately decreasing Mg# exhibited by the altered grains (*chr-2* trend; Fig. 5a, b) is due to the loss of Mg, Al and Cr, and enrichment in Fe^{3+}, during alteration of the chromite

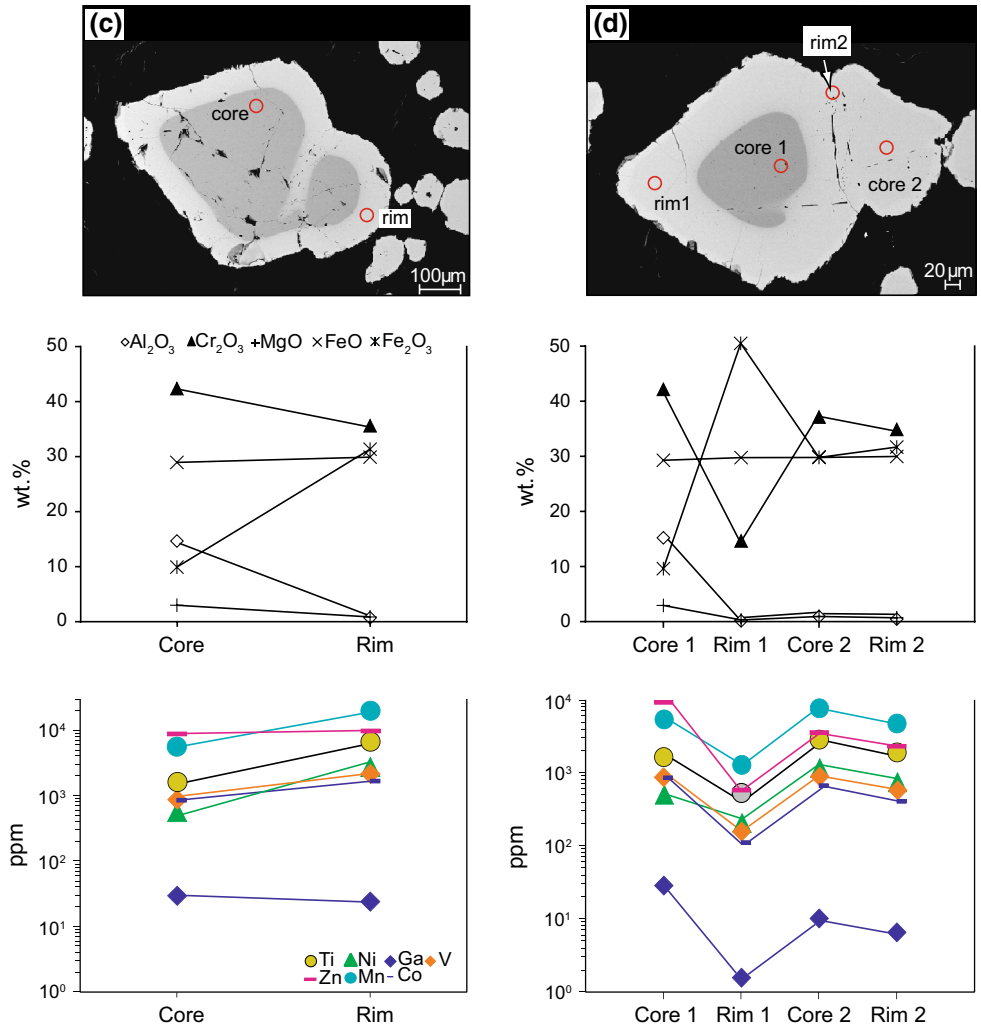

Fig. 6 continued

grain to ferritchromit (Mukherjee et al. 2010) (Appendix B—available online). The cores of the altered chromite grains also have experienced modification, and they plot either close to or within the field of chromites from metamorphosed komatiites, while some core compositions show extreme Al-loss during alteration (Fig. 5b). Most of the altered chromite grains from the lower and upper chromitite units in the Nuggihalli greenstone belt show similar patterns of trace-element distribution and an overall enrichment in Zn, Ga, Mn and V compared to the unaltered grains (Fig. 6b–f; Table 1), indicating that the enrichment is linked to secondary alteration processes. Also, enrichment of these elements in the cores of the altered grains indicates that the core has been modified during the alteration process. During alteration, the trivalent cations Ga and V decrease from the core to the rim concomitantly with Cr, while Fe^{3+} and Ti^{4+} are enriched in the rim. This indicates that Ga and V behave similarly to Cr and are being substituted by Fe^{3+} and Ti during alteration. In general, Ga behaves similarly to Fe^{3+} due to their similar ionic radii (e.g., Dare et al. 2009), and hence, these elements can substitute for one another. Such primary substitution is observed in the unaltered chromite grains from this study where the Ga concentration in the grains correlates with Fe^{3+}# ($100 \times Fe^{3+}/(Cr + Al + Fe^{3+})$) (Fig. 10a). Ga also shows positive correlations with Al_2O_3 in the unaltered chromite grains, indicating that it can substitute for Al^{3+} but not Cr^{3+}, as a negative correlation is observed with the latter (Fig. 10b, c). In the altered grains, the divalent cations Zn and Mn behave similarly to Mg during alteration; they show lower concentrations in the rims and are substituted by Ni, which is enriched in the rim (Fig. 6b, e). The Ni concentrations in the core of the altered (114–571 ppm; Table 1) as well as the unaltered chromite grains (661–1203 ppm; Table 1) from this study are comparable with the range of values found in chromites from podiform

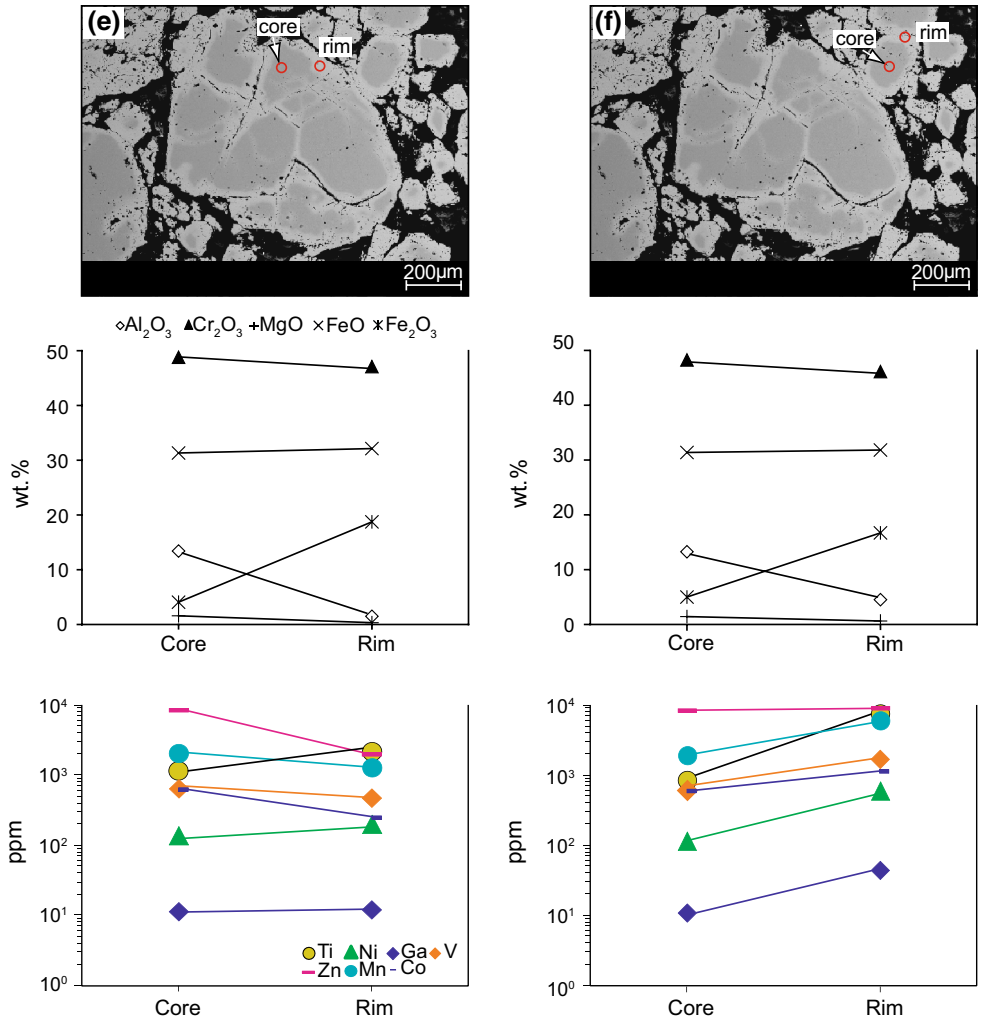

Fig. 6 continued

chromitites (441–875 ppm) of the Thetford ophiolite (Pagé and Barnes 2009). However, some of the altered rims in chromites from this study show very high concentrations of Ni (2362–3584 ppm; Table 1), indicating its enrichment during the alteration process.

Although most of the altered chromite grains have similar trace-element distribution patterns, there are some differences. The inter-grain and inter-sample variations in the trace-element patterns of chromite grains help to confirm our earlier finding that the alteration of chromite to ferritchromit and magnetite is heterogeneous and related to hydrothermal activity during serpentinization (Mukherjee et al. 2010). The fluids responsible for serpentinization were perhaps responsible for the addition of Ni (from altering olivine), Co and Ti in the altered grains. The local presence of carbonates was responsible for the enrichment of Zn and Mn in some grains (e.g., Barnes 2000). The enrichment of all trace elements in Grain 2 of DHR-10-120 (Fig. 6f) may reflect the higher mode of carbonate in this sample (≈25–35 modal percent of magnesite) compared to the other chromitites, and the predominance of interstitial carbonate around this grain compared to Grain 1 of the same sample (Fig. 6e). This observation suggests that different fluid media (during serpentinization) have the effect of changing the trace-element distribution pattern in the chromite grains; carbonate-rich fluids are reactive enough to alter chromite. In the Nuasahi Massif (Singhbhum craton, eastern India), low-temperature secondary carbonate-rich fluids have completely altered chromite grains to form the hydrous chrome carbonate, stichtite [$Mg_6Cr_2(OH)16CO_3{\cdot}4H_2O$], which commonly occurs in chromitites and in serpentinized dunite and peridotite. Stichtite occurs predominantly as veinlets or along fractures in chromite grains, but in dunites it may completely pseudomorph chromite grains (Mondal and Baidya 1996).

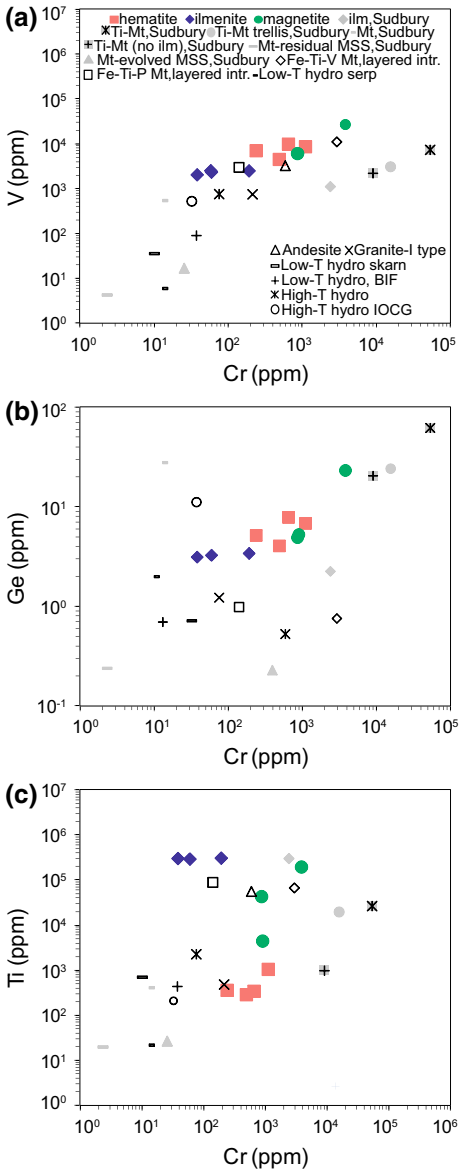

Fig. 7 Binary variation diagrams of trace elements in Fe–Ti oxides from magnetites of the Nuggihalli greenstone belt **a** Cr versus V, **b** Cr versus Ge, **c** Cr versus Ti. Data from this study are compared with magnetites from different occurrences. Data for the oxides are from Dare et al. (2014) and oxides associated with massive sulfides are from Dare et al. (2012)

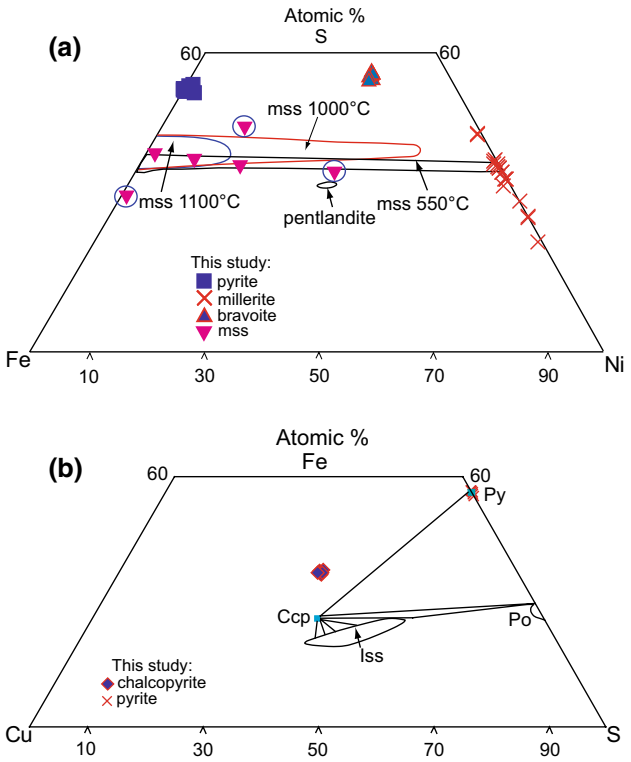

Fig. 8 **a** Fe–Ni–S ternary plot of Kullerud et al. (1969) utilized to show the compositional fields of interstitial pyrite and bravoite from magnetites, MSS inclusions within pyroxenite and interstitial millerite from massive chromitite of the Nuggihalli greenstone belt, **b** Cu–Fe–S ternary plot (Craig and Scott 1974) showing the compositional field for interstitial chalcopyrite and pyrite within magnetites from the Nuggihalli greenstone belt. Mss: monosulfide solid solution; Ccp: chalcopyrite; Py: pyrite; Po: pyrrhotite; Iss: intermediate solid solution

Trace-element fingerprint of magnetite

Trace-element data for magnetites (remnant), ilmenites and hematite from Nuggihalli are compared with data for magmatic Fe–Ti–V–P-rich magnetites from the upper parts of layered intrusions like the Bushveld Complex (South Africa) and the Sept Iles (Canada), from intermediate and felsic magmas like andesite and Granite-I type magmas, from high- (>500 °C) and low-temperature (<500 °C) hydrothermal fluids (Dare et al. 2014) and from massive Ni–Cu (PGE)-rich deposits like Sudbury (Dare et al. 2012).

In the Cr versus V diagram, the remnant magnetites plot closer to the magmatic Fe–Ti–V-rich magnetites and magnetites crystallizing from andesitic melts, while the ilmenites plot closer to the Fe–Ti–P-rich magnetites (Fig. 7a). A similar distribution is apparent in the Cr versus Ti diagram (Fig. 7c); however, in this figure the hematites plot in the range of magnetites crystallizing from hydrothermal fluids and Granite-I type magmas. No such pattern is recognizable in the Cr versus Ge diagram (Fig. 7b). The remnant magnetites from this study show higher Ti concentrations than the titanomagnetites associated with massive sulfides from Sudbury, with or without ilmenite exsolution (Dare et al. 2012) (Fig. 7c). In general, the oxides from massive sulfides of the Sudbury Igneous Complex (Dare et al. 2012) have lower concentrations of V and Ti and highly variable contents of Cr and Ga compared to the oxides from this study. These indicate that the magnetites from Nuggihalli have crystallized from a fractionated and relatively evolved

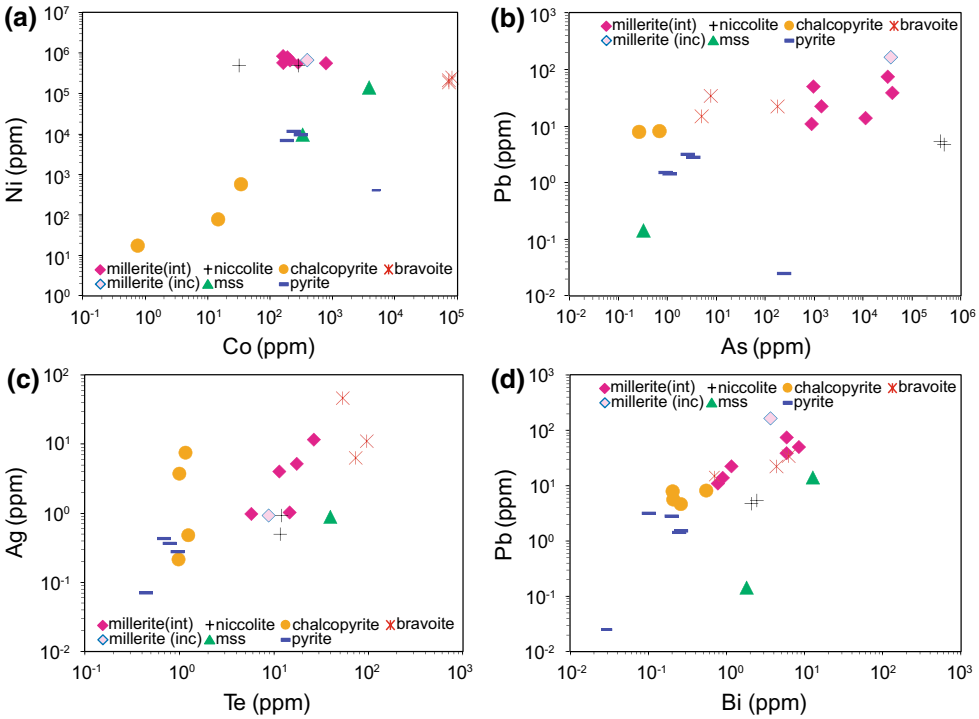

Fig. 9 Binary variation diagrams of trace elements in sulfides **a** Co versus Ni, **b** As versus Pb, **c** Te versus Ag, **d** Bi versus Pb

silicate melt rather than a high-temperature sulfide melt and have exsolved ilmenite during cooling. The high Ti concentrations in magnetites from Nuggihalli (Fig. 7c; Table 2) indicate their crystallization from a Ti-rich fractionated mafic or gabbroic magma. The V contents of the magnetite and ilmenite grains from our study are also high (Table 2); this indicates an oxygen fugacity near QFM, because high oxygen fugacity promotes the maximum partitioning of vanadium into magnetite (Toplis and Corgne 2002).

Trace-element fingerprint of sulfides

In Fig. 8a, the compositions of sulfide inclusions within pyroxenite are seen to be representative of monosulfide solid solution (MSS) that segregated between 1000 and 1100 °C (Fig. 8a). MSS is the high-temperature primary sulfide that exsolves from a silicate melt on attainment of sulfide saturation (Kullerud et al. 1969). This indicates that despite alteration and metamorphism in the host rock, the primary compositions of sulfide were retained within the pyroxenes (now altered to actinolite). However, some of the MSS compositions have undergone sub-solidus re-equilibration during later alteration and metamorphism of the host rock, producing a scatter about the MSS field in Fig. 8a.

Millerites (NiS) mostly represent a low-temperature sulfide (<379 °C; Kullerud et al. 1969) that forms as a replacement of nickel-bearing sulfides (e.g., pentlandite and pyrrhotite), while bravoite ($FeNiS_2$) and niccolite (NiAs) are low-temperature sulfides commonly formed during hydrothermal alteration (Kullerud et al. 1969). In the Cu–Fe–S diagram (Fig. 8b), the chalcopyrites from our study do not fall in the expected field of chalcopyrite but show higher concentrations of Fe, which may be due to sub-solidus re-equilibration with the host magnetite. On the contrary, the composition of pyrite from our study is apparently unaffected, as it plots in the expected pyrite field in Fig. 8b. The enrichments of Ni, Co, Te, As and Bi in millerite, niccolite and bravoite relative to chalcopyrite and pyrite imply that the enrichment was related to low-temperature hydrothermal processes such as the alteration that generated serpentinite in the ultramafic–mafic complex (Fig. 9a–d). The re-equilibrated MSS also shows increased concentrations of these elements compared to its primary unaltered counterpart (Fig. 9a–d). The high concentrations of Ag and Pb in chalcopyrite and pyrite (Fig. 9b–d) are expected, because these formed from a Cu–Fe-rich residual sulfide melt that evolved and fractionated from a primary high-temperature MSS, thus becoming progressively enriched in incompatible chalcophile and chalcogenide elements (Skinner et al. 1976).

PGEs are below the detection limit in all types of sulfides, with a few exceptions (Table 3). PGEs (Os, Ir, Ru, Rh, Pt, Pd) are chalcophile elements and should fractionate into a sulfide phase owing to their large partition coefficient into the sulfide phase ($D_{PGE}^{\text{sulfide-silicate melt}} \approx 10^3$–$10^8$; Stone et al. 1990; Peach and Mathez 1996; Fleet et al. 1999; Sattari et al. 2002). In the Nuggihalli greenstone belt, the sulfides

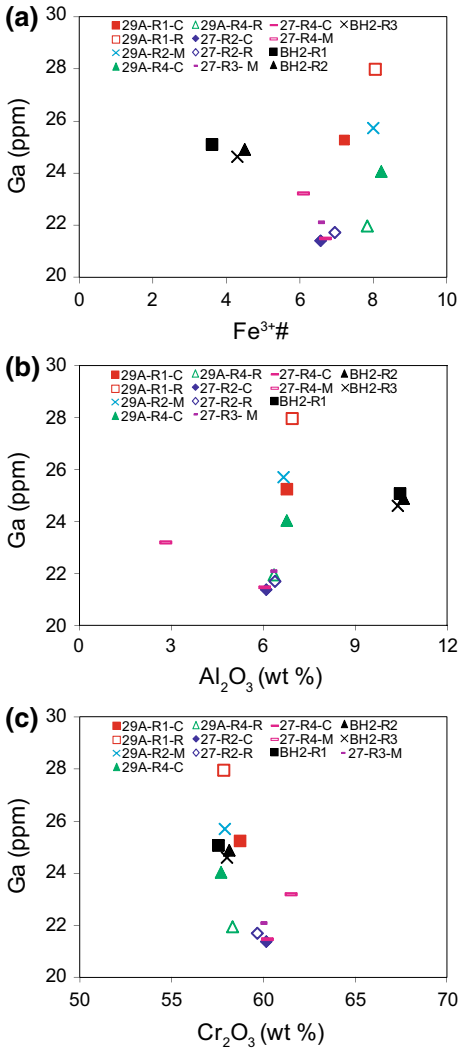

Fig. 10 **a** Fe^{3+}# versus Ga, **b** Al_2O_3 versus Ga and **c** Cr_2O_3 versus Ga in unaltered chromites from massive chromitites of Byrapur and Bhaktarhalli. The abbreviations C, R and M refer to the core, rim and middle part of the chromite grains

in massive chromitites (e.g., millerite and niccolite) and in magnetites (e.g., bravoite) are secondary low-temperature sulfides that cannot control the distribution of PGE. Moreover, sulfide saturation occurred late in the magmatic crystallization history of the layered sill-like ultramafic–mafic rocks, i.e., during formation of pyroxenites in the Nuggihalli greenstone belt (Mukherjee et al. 2014). The IPGEs (Os, Ir, Ru) were fractionated by PGMs (e.g., laurite) included in earlier crystallizing chromite within massive chromitites, thus depleting the sulfides (e.g., MSS within pyroxene in the pyroxenites and chalcopyrite and pyrite in magnetite) in the same elements. Moreover, the metavolcanic komatiitic schists in the Nuggihalli greenstone belt are extremely PGE-depleted, thus suggesting the mantle source was also depleted in PGE (Mukherjee et al. 2014).

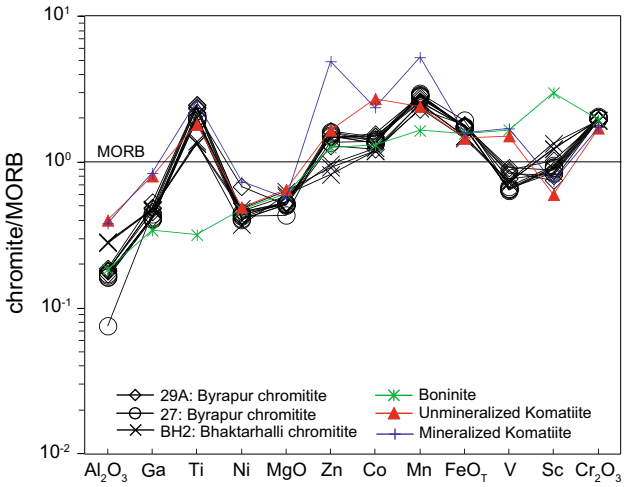

Fig. 11 MORB-normalized trace and major elements in unaltered chromites from massive chromitites of Byrapur and Bhaktarhalli in the Nuggihalli greenstone belt that are compared with chromite compositions associated with magmas like boninites (Bonin Islands; Pagé and Barnes 2009), nickel–sulfide unmineralized (McAuliffe Well, Round Hill, Wiluna, Yunndage; Yilgarn craton, Western Australia; Yao 1999) and mineralized komatiites (Honeymoon Well, Snake Hill; Yilgarn craton, Western Australia; Yao 1999)

Constraints on parental magma composition and probable tectonic setting in the Mesoarchean

The compositions of unaltered chromites from Nuggihalli can be used to fingerprint the composition of their parental magma and relate it to a tectonic setting (e.g., Mondal et al. 2006). The unaltered chromites show the *chr-1* trend of variable Mg# at constant Cr# (Fig. 5a) that is characteristic of chromites in layered intrusions and reflects fractional crystallization (Mukherjee et al. 2010 and references therein). The cores of these grains are apparently unaffected by secondary alteration and metamorphism as they follow the magmatic (*chr-1*) trend (Fig. 5b). Although the Bhaktarhalli chromites plot in the field of chromites from metamorphosed (greenschist facies) komatiites, this does not mean that they are altered but reflects the overlap of the Cr# of these chromites with the uppermost limit of Cr# in the altered chromites from metamorphosed komatiites (Fig. 5b). The trace-element data from these chromites were used to evaluate the composition of the parental magma. In Fig. 11, the contents of trace elements and selected major elements in unaltered chromites from Byrapur and Bhaktarhalli are compared with high-Mg parental melts like boninites (Bonin Islands; Pagé and Barnes 2009) and nickel–sulfide mineralized and unmineralized komatiites (Norseman-Wiluna greenstone belt, Yilgarn craton; Yao 1999). The data have been normalized to MORB as no significant variation in trace-element abundances was observed between our chromites and the different parental

melts chosen for comparison, when the normalization was done using chondrites or the primitive mantle. The trace-element data for the unaltered chromites from this study most closely resemble the pattern of komatiites that lack nickel–sulfide mineralization (Fig. 11).

The above results are consistent with the conclusions derived from a previous EPMA-based mineralogical study of these unaltered chromites (Mukherjee et al. 2010), where the Al_2O_3 (wt%), TiO_2 (wt%) and FeO/MgO ratio of the parental melt was calculated using the composition of unaltered Nuggihalli chromites and the relationships of Maurel and Maurel (1982) and Kamenetsky et al. (2001). The computed parental melt was found to resemble komatiites and komatiitic basalts reported from early Archean greenstone belts (Sargur Group) in the Western Dharwar craton (Mukherjee et al. 2010).

Dare et al. (2009) studied the trace-element compositions (using LA-ICPMS) of chromites in mantle peridotites from oceanic and ophiolite settings, and introduced the Ga/Fe^{3+}# versus Ti/Fe^{3+}# diagram that could efficiently differentiate between chromites that formed in a suprasubduction zone (SSZ) environment from those that formed in a mid-ocean ridge (MOR) setting. This diagram could further differentiate between chromites that were hosted in residual peridotites (e.g., harzburgites), from those that were hosted in rocks formed by melt–rock interaction (e.g., dunite), in any of these tectonic settings. However, according to the authors this tectonic discrimination diagram should not be used for chromitite and lava spinels, as their history of subsolidus exchange is different to that of the peridotites. Dare et al. (2009) suggest that future work should determine the boundaries for chromitite and lava spinels. Presently, this is a limitation as there is a very small database available for in situ trace elements in chromite. Despite the constraints, we tried to plot unaltered chromites from massive chromitite of Nuggihalli in the Ga/Fe^{3+}# versus Ti/Fe^{3+}# diagram of Dare et al. (2009), where we found that the Byrapur chromites plot in the SSZ field while those from Bhaktarhalli plot in the MOR field (Fig. 12). It is interesting to note that these observations match with our previous mineralogical study on these unaltered chromites (Mukherjee et al. 2010), where tectonic discrimination diagrams using major-element data in chromite (e.g., Cr ratio vs. Mg ratio; Cr–Al–Fe^{3+}; Al_2O_3 vs. TiO_2) indicated their derivation from SSZ settings. Also, in terms of their major elements (e.g., MgO, Al_2O_3 and TiO_2), the chromites from these two places showed differences in composition such that the parental magma compositions calculated using the Bhaktarhalli chromites were found to be Mg- and Al-rich and matched more with the composition of Archean high-Mg siliceous basalt (Mukherjee et al. 2010) considered to be equivalent to boninites (Parman et al. 2001; Mondal et al. 2006 and references therein). Based on the above results, a probable geodynamic model for the sill-like chromitite-bearing ultramafic–mafic rocks in the Nuggihalli greenstone belt is presented in Fig. 13.

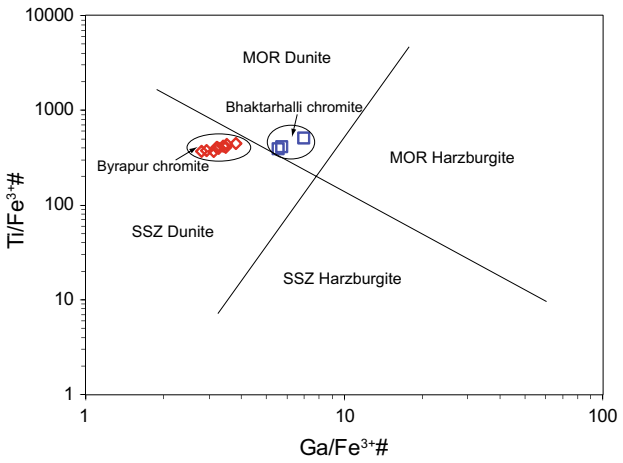

Fig. 12 Unaltered chromite compositions from the Byrapur and Bhaktarhalli mines plotted in the Ga/Fe^{3+}# versus Ti/Fe^{3+}# tectonic discrimination plot of Dare et al. (2009). The Byrapur chromites plot in the SSZ field and the Bhaktarhalli chromites plot in the MOR field

Partition coefficients of trace elements in chromite and magnetite

Based on the in situ trace-element data, a quantitative estimate of the partition coefficients of trace elements between chromite and komatiitic melts from Archean greenstone belts can be derived (Appendix G—available online). Any partition coefficient calculation is based on the assumption that the crystal and melt were in equilibrium. In our case since the actual melt composition is not preserved in the Nuggihalli greenstone belt, it is very difficult to obtain the real partition coefficient values for the trace elements. However, we have tried to estimate what the partition coefficients of trace elements would be, assuming komatiitic and boninitic parental melts. The reason for comparing with the former is that the parental melt composition using unaltered chromite data, as well as the closely associated metavolcanic rocks in the greenstone belt, hints at komatiitic compositions. Boninites have been used because of their SSZ lineage and because calculation of parental magmas for Bhaktarhalli chromite yielded a high-Mg siliceous basalt that is compositionally similar to boninites. The partition coefficients were calculated using the equation $D = C^{i}_{chromite}/C^{i}_{melt}$, where $C^{i}_{chromite}$ is the concentration of trace element 'i' in chromite from the Nuggihalli massive chromitites, and C^{i}_{melt} is the concentration of trace elements in komatiites and boninites (Appendix G, H—available online). Since massive chromitites are being studied, the mineral partition coefficient can be considered to be similar to the bulk distribution coefficient, as

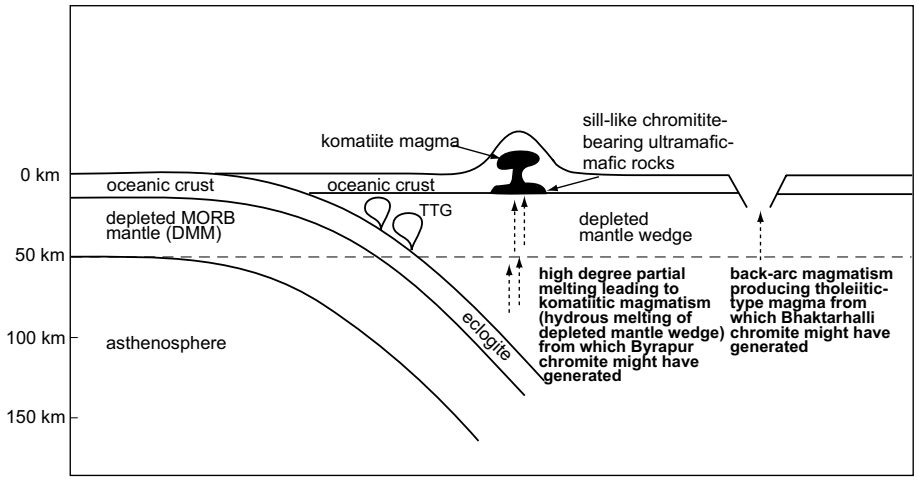

Fig. 13 Model showing the probable geodynamic setting of the chromitite-bearing sill-like ultramafic–mafic rocks, surrounding metavolcanic schists and the TTG in the Western Dharwar craton (after Mukherjee et al. 2012)

chromite was the only crystallizing phase (liquidus phase) from the melt that accumulated to form the massive chromitites (e.g., Irvine 1977; Mondal and Mathez 2007). The partition coefficients were calculated with both Al-depleted and undepleted komatiites ranging from early to late Archean (Appendix G—available online). The partition coefficient calculations show that Ga (D = 4.4–5.2), V (D = 2.4–6.6), Co (D = 1.5–3.0) and Zn (D = 3.6–11) are compatible in chromites, while Mn (D = 0.9–1.7) and Ti (D = 0.9–1.3) are less strongly so (Appendix G—available online), and Ni and Sc are incompatible. The partition coefficients calculated with late Archean boninitic melts and boninites from Cape Vogel (Appendix H—available online) show similar results where V (D = 1.9–3.9) and Co (D = 3.2–4.6) are compatible in chromite, while Mn (D = 0.7–2.2) and Ti (D = 0.4–1.7) are less compatible. The only contrast in case of boninites is that Ni is observed to be compatible (D = 2.8–5.3) in chromite. The altered chromites have a highly variable range of partition coefficients with a few altered rims showing extremely large D values for Zn, V, Co, Mn and Ni which are an artifact of alteration (Appendix G, H—available online). It is interesting to note that carbonate alteration in chromites (e.g., Grain 2, DHR-10-120) enhances the incorporation of Sc (Appendix G, H—available online). Although a distinct trend is not apparent, alteration in chromites seems to enhance incorporation of Ti and loss of Ga (Appendix G, H—available online).

We have compared our estimated D values with the empirical partition coefficients calculated by Pagé and Barnes (2009) for accessory chromite–boninite (boninite from Thetford Mine ophiolite and Bonin Island; Appendix H—available online); the patterns are found to be similar, but the exact values of partition coefficients vary.

Recently, Klemme et al. (2013) conducted experiments to constrain the partition coefficients of trace elements between spinel and basaltic melt at 1 atm, 1200°–1430 °C and fO_2 between log −12 and −0.7. The authors observed that the trivalent cations in the spinel structure control the partitioning of Ti, Sc and the high-field-strength elements (HFSE) such that their concentration is highest in Fe^{3+}-enriched spinel, followed by the Cr- and Al-enriched spinel species. The data from the Nuggihalli chromites show that Ti is moderately compatible in the chromite structure and becomes more compatible with alteration and enrichment of Fe^{3+} in the chromite structure (Appendix G, H—available online); Sc is always incompatible except in case of chromites with ambient interstitial carbonates (Appendix G, H—available online). The concentrations of most HFSEs (e.g., Zr, Nb, Hf, Ta) are below the detection limits for the Nuggihalli chromites.

Trace-element partition coefficient data for magnetites hosted in greenstone belts are presented for the first time in this study (Appendix I—available online). However, the D values that are presented here do not necessarily represent the magmatic distribution of trace elements between the oxide phases, as the magnetite has been hydrothermally altered and compositionally re-equilibrated. Previous work has mostly dealt with experimentally determined partition coefficients of HFSEs and V between magnetite and basaltic melts (e.g., Nielsen and Beard 2000; Toplis and Corgne 2002), and partition coefficients of trace elements between co-existing sulfides and accessory magnetites from massive sulfide deposits such as the Sudbury Igneous Complex (Dare et al. 2012). In this study, partition coefficients of trace elements have been calculated between magnetite, ilmenite, hematite and an assumed komatiitic basaltic melt (Fan and Kerrich 1997). Komatiitic basalt was used in the calculations owing to the evolved nature of the melt from which magnetite crystallizes. The D values indicate that distribution of Sc (D = 3.0–3.6), Ti (D = 88.9–93.5), Mn (D = 2.4–4.1) and Nb (D = 4.3–5.1) is controlled by ilmenite (Appendix I—available online). Ti, Mn and Nb are compatible (D^{Ti} = 13.1–59.3; D^{Mn} = 2.8; D^{Nb} = 3.1) in remnant magnetites but now reside in exsolved lamellae of ilmenite. Both magnetite and

hematite control the distribution of V (D = 15.3–24.8). V is also compatible in ilmenite, but the D values are slightly less (D = 9.4–11.6) relative to hematite and magnetite. The HFSEs and Cr are strongly incompatible in magnetite, ilmenite (except Nb) and hematite (Appendix I—available online).

Conclusions

1. In situ trace-element analysis of unaltered chromite from massive chromitites indicates that the parental magma of the chromitite ore-bodies was a komatiite without nickel–sulfide mineralization. The Ga/Fe^{3+}# versus Ti/Fe^{3+}# plot based on in situ data of unaltered chromites suggests arc (Byrapur deposit) and rift-like (Bhaktarhalli) environments for the Nuggihalli chromite deposit. The results from this study are consistent with our previous inferences based on major-element data, which suggested a SSZ environment in the Archean.
2. In situ trace-element study of altered and compositionally zoned chromite grains showed a decrease in concentrations of Ga, V, Co, Zn, Mn and enrichment of Ni and Ti in the ferritchromit rim. The intra-grain, inter-grain and inter-sample variations in trace-element distribution in the altered chromites are attributed to serpentinization.
3. Estimated partition coefficients (D) of trace elements between unaltered chromites from our study and high-Mg magmas like komatiite and boninite indicate compatibility of Ga, V, Zn and Co that are compatible in chromite, while Ti and Mn are less strongly compatible. Ni is found to be more compatible in chromites in boninitic melts compared to komatiites. Carbonate alteration in chromites seems to enhance incorporation of Sc.
4. In situ trace-element analyses of magnetite suggest similarity with magmatic magnetites from Fe–Ti–V-rich magnetite bands in layered intrusions and those crystallizing from andesitic melts. The latter suggests that the parental silicate melt was quite evolved during crystallization of the magnetite.
5. Trace-element analyses of sulfides indicate enrichment of Ni, Co, Te, As and Bi in millerite, niccolite and bravoite during serpentinization. Inclusions of MSS in pyroxenite, and pyrite and chalcopyrite inclusions in magnetite, retain primary characteristics, except for Fe-enrichment in chalcopyrite by sub-solidus re-equilibration with magnetite grains. All types of disseminated sulfides are depleted in PGE due to late sulfide saturation and the PGE-depleted nature of the mantle source for the sill-like ultramafic–mafic plutonic rocks and the surrounding metavolcanic schists in the Nuggihalli greenstone belt.

Acknowledgments This work is a contribution under a collaborative exchange project between Sisir Mondal (Jadavpur University, India) and William Griffin and Suzanne O'Reilly (Macquarie University, Australia) under which Ria Mukherjee received laboratory training and acquired data for her PhD thesis from the ARC Centre of Excellence from Core to Crustal Fluids (CCFS) and GEMOC through a visiting program. This is contribution 640 from the ARC Centre of Excellence for Core to Crust Fluid Systems (http://www.ccfs.mq.edu.au) and 1017 in the GEMOC Key Centre (http://www.gemoc.mq.edu.au). The analytical data were obtained using instrumentation funded by DEST Systematic Infrastructure Grants, ARC LIEF, NCRS/AuScope, industry partners and Macquarie University. Kevin Grant and William Powell are thankfully acknowledged for their assistance with EPMA-SEM and LA-ICPMS, respectively. Ria Mukherjee wishes to acknowledge CSIR (New Delhi) for a Senior Research Fellowship. Fieldwork support was from UKIERI-UGC Thematic Partnership 2013 (Project Reference F.No.184-1/2013). Tim Grove is acknowledged for his encouraging editorial handling of the manuscript. Steve Parman and an anonymous reviewer of the journal are acknowledged for their constructive review of the article.

References

Abzalov MZ (1998) Chrome spinels in gabbro-wehrlite intrusions of the Pechenga area, Kola Peninsula, Russia: emphasis on alteration features. Lithos 43:109–134

Ahmed AH, Arai S (2002) Unexpectedly high-PGE chromitite from the deeper mantle section of the northern Oman ophiolite and its tectonic implications. Contrib Mineral Petrol 143:263–278

Alard O, Griffin WL, Lorand JP, Jackson SE, O'Reilly SY (2000) Non chondritic distribution of the highly siderophile elements in mantle sulphides. Nature 407:891–894

Arai S, Ahmed AH (2013) Secular change of the chromite concentration process from the Archean to Phanerozoic. Goldschmidt abstract. Min Mag, p 606

Barnes SJ (2000) Chromite in komatiites, II. Modification during greenschist to mid amphibolite facies metamorphism. J Petrol 41:387–409

Barnes SJ, Roeder PL (2001) The range of spinel compositions in terrestrial mafic and ultramafic rocks. J Petrol 42:2279–2302

Barnes SJ, Lesher CM, Keays RR (1995) Geochemistry of mineralised and barren komatiites from the Perseverance nickel deposit, Western Australia. Lithos 34:209–234

Bliss NW, MacLean WH (1975) The paragenesis of zoned chromite from central Manitoba. Geochim Cosmochim Acta 39:973–990

Buddington AF, Lindsley DH (1964) Iron–titanium oxide minerals and synthetic equivalents. J Petrol 5:310–357

Burkhard DJM (1993) Accessory chromian spinels: their coexistence and alteration in serpentinites. Geochim Cosmochim Acta 57:1297–1306

Colás V, González-Jiménez JM, Griffin WL, Fanlo I, Gervilla F, O'Reilly SY, Pearson NJ, Kerestedjian T, Proenza JA (2014) Fingerprints of metamorphism in chromite: new insights from minor and trace elements. Chem Geol 389:137–152

Craig JR, Scott SD (1974) Sulfide phase equilibria. Mineral Soc Am Short Course Notes 1:1–110

Dare SAS, Pearce JA, McDonald I, Styles MT (2009) Tectonic discrimination of peridotites using fO_2–Cr# and Ga–Ti–Fe^{III} systematics in chrome-spinel. Chem Geol 261:199–216

Dare SAS, Barnes S-J, Prichard HM, Fisher PC (2011) Chalcophile and platinum-group element (PGE) concentrations in the sulfide minerals from the McCreedy East deposit, Sudbury, Canada, and the origin of PGE in pyrite. Miner Depos 46:381–407

Dare SAS, Barnes S-J, Beaudoin G (2012) Variation in trace element content of magnetite crystallized from a fractionating sulfide

liquid, Sudbury, Canada: implications for provenance discrimination. Geochim Cosmochim Acta 88:27–50

Dare SAS, Barnes S-J, Beaudoin G, Méric J, Boutroy E, Potvin-Doucet C (2014) Trace elements in magnetite as petrogenetic indicators. Miner Depos 49:785–796

Devaraju TC, Viljoen RP, Sawkar RH, Sudhakara TL (2009) Mafic and ultramafic magmatism and associated mineralization in the Dharwar craton, southern India. J Geol Soc India 73:73–100

Dick HJB, Bullen T (1984) Chromian spinel as a petrogenetic indicator in abyssal and alpine type peridotites and spatially associated lavas. Contrib Mineral Petrol 86:54–76

Evans BW, Frost BR (1975) Chrome-spinel in progressive metamorphism—a preliminary analysis. Geochim Cosmochim Acta 39:959–972

Fan J, Kerrich R (1997) Geochemical characteristics of aluminum depleted and undepleted komatiites and HREE-enriched low-Ti tholeiites, western Abitibi greenstone belt: a heterogeneous mantle plume-convergent margin environment. Geochim Cosmochim Acta 61:4723–4744

Fleet ME, Crocket JH, Liu M, Stone WE (1999) Laboratory partitioning of platinum-group elements (PGE) and gold with application to magmatic sulfide–PGE deposits. Lithos 47:127–142

Gervilla F, Padrón-Navarta J, Kerestedjian T, Sergeeva I, González-Jiménez JM, Fanlo I (2012) Formation of ferrian chromite in podiform chromitites from the Golyamo Kamenyane serpentinite, Eastern Rhodopes, SE Bulgaria: a two-stage process. Contrib Mineral Petrol 164:1–15

González-Jiménez JM, Locmelis M, Belousova E, Griffin WL, Gervilla F, Kerestedjian TN, Pearson NJ, Sergeeva I (2013) Genesis and tectonic implications of podiform chromitites in the metamorphosed Ultramafic Massif of Dobromirtsi (Bulgaria). Gondwana Res 27:555–574

González-Jiménez JM, Griffin WL, Gervilla F, Proenza JA, O'Reilly SY, Pearson NJ (2014) Chromitites in ophiolites: how, where, when, why? Part II. The crystallization of chromitites. Lithos 189:140–158

Griffin WL, Powell WJ, Pearson NJ, O'Reilly SY (2008) GLITTER: data reduction software for laser ablation ICP-MS. In: Sylvester P (ed) Laser ablation-ICP–MS in the earth sciences: current practices and outstanding issues. Mineral Assoc Can Short Course 40:308–311

Haggerty SE (1991) Oxide textures—a mini-atlas. In: Lindsley DH, Ribbe PH (eds) Oxide minerals: petrologic and magnetic significance. Rev Mineral 25:129–219

Hamlyn PR, Keays RR (1979) Origin of chromite compositional variation in the Panton Sill, Western Australia. Contrib Mineral Petrol 69:75–82

Hickey RL, Frey FA (1982) Geochemical characteristics of boninite series volcanics: implications for their source. Geochim Cosmochim Acta 46:2099–2115

Irvine TN (1965) Chromian spinel as a petrogenetic indicator. Part I, theory. Can J Earth Sci 2:648–671

Irvine TN (1967) Chromian spinel as a petrogenetic indicator. Part II, petrographic applications. Can J Earth Sci 4:71–103

Irvine TN (1977) Origin of chromitite layers in the Muskox intrusion and other layered intrusions: a new interpretation. Geology 5:273–277

Jackson ED (1969) Chemical variation in coexisting chromite and olivine in chromitite zones of the Stillwater complex. Econ Geol Monogr 4:41–71

Jafri SH, Khan N, Ahmed SM, Saxena R (1983) Geology and geochemistry of Nuggihalli schist belt, Dharwar craton, Karnataka, India. In: Naqvi SM, Rogers JJW (eds) Precambrian of South India. Memoir Geol Soc India 4:110–120

Kamenetsky VS, Crawford AJ, Meffre S (2001) Factors controlling chemistry of magmatic spinel: an empirical study of associated olivine, Cr-spinel and melt inclusions from primitive rocks. J Petrol 42:655–671

Kerrich R, Wyman D, Fan J, Bleeker W (1998) Boninite series; low Ti-tholeiite associations from the 2.7 Ga Abitibi greenstone belt. Earth Planet Sci Lett 164:303–316

Klemme S, Wijbrans CH, Vollmer C, Menneken M, Berndt J (2013) Experimental study of trace element partitioning between spinel and silicate melts: effects of oxygen fugacity and spinel composition. Goldschmidt abstract. Min Mag, p 1476

Kullerud G, Yund RA, Moh GH (1969) Phase relations in the Cu–Fe–S, Cu–Ni–S and Fe–Ni–S systems. In: Wilson HDB (ed) Magmatic ore deposits. Econ Geol Pub, Lancaster, pp 323–343

Leelananadam C, Burke K, Ashwal LD, Webb SJ (2006) Proterozoic mountain building in Peninsular India: an analysis based primarily on alkaline rock distribution. Geol Mag 143:1–18

Loferski PJ, Lipin BR (1983) Exsolution in metamorphosed chromite from the Red Lodge district, Montana. Am Mineral 68:777–789

Maurel C, Maurel P (1982) Etude expérimentale de la solubilité du chrome dans les bains silicatés basiques et sa distribution entre liquide et minéraux coexistants: conditions d'existence du spinelle chromifére. Bull Mine´ral 105:197–202

Mondal SK, Baidya TK (1996) Stichtite [$Mg_6Cr_2(OH)_{16}CO3{\cdot}4H_2O$] in Nausahi ultramafites, Orissa, India—its transformation at elevated temperatures. Min Mag 60:832–840

Mondal SK, Mathez EA (2007) Origin of the UG2 chromitite layer, Bushveld complex. J Petrol 48:495–510

Mondal SK, Ripley EM, Li C, Frei R (2006) The genesis of Archean chromitites from the Nuasahi and Sukinda Massifs in the Singhbhum craton, India. Precambrian Res 148:45–66

Mukherjee R, Mondal SK, Rosing MT, Frei R (2010) Compositional variations in the Mesoarchean chromites of the Nuggihalli schist belt, Western Dharwar craton (India): potential parental melts and implications for tectonic setting. Contrib Mineral Petrol 160:865–885

Mukherjee R, Mondal SK, Frei R, Rosing MT, Waight TE, Zhong H, Ravindra Kumar GR (2012) The 3.1 Ga Nuggihalli chromite deposits, Western Dharwar craton (India): geochemical and isotopic constraints on mantle sources, crustal evolution and implications for supercontinent formation and ore mineralization. Lithos 155:392–409

Mukherjee R, Mondal SK, Zhong H, Bai Z-J, Balaram V, Ravindra Kumar GR (2014) Platinum group element geochemistry of komatiite-derived 3.1 Ga ultramafic–mafic rocks and chromitites from the Nuggihalli greenstone belt, Western Dharwar craton (India). Chem Geol 386:190–208

Murthy NGK (1987) Mafic dyke swarms of the Indian shield, Mafic swarms. Geol Assoc Can Spec Pap 34:393–400

Nielsen RL, Beard JS (2000) Magnetite-melt HFSE partitioning. Chem Geol 164:21–34

Norman MD, Pearson NJ, Sharma A, Griffin WL (1996) Quantitative analysis of trace elements in geological materials by laser ablation ICPMS: instrumental operating conditions and calibration values of NIST glasses. Geostand Newslett 20:247–261

Pagé P, Barnes S-J (2009) Using trace elements in chromites to constrain the origin of podiform chromitites in the Thetford Mines ophiolite, Québec, Canada. Econ Geol 104:997–1018

Pagé P, Barnes S-J, Bédard JH, Zientek ML (2012) In situ determination of Os, Ir, and Ru in chromites formed from komatiite, tholeiite and boninite magmas: implications for chromite control of Os, Ir and Ru during partial melting and crystal fractionation. Chem Geol 302(303):3–15

Parman SW, Grove TL, Dann JC (2001) The production of Barberton komatiites in an Archean subduction zone. Geophys Res Lett 28:2513–2516

Peach CL, Mathez EA (1996) Constraints on the formation of platinum-group element deposits in Igneous Rocks. Econ Geol 91:439–450

Pouchou JL, Pichoir F (1984) A new model for quantitative X-ray microanalysis. Part 1. Applications to the analysis of homogeneous samples (English edition). Rech Aerosp 3:11–38

Puchtel IS, Blichert-Toft J, Touboul M, Walker RJ, Byerly GR, Nisbet EG, Anhaeusser CR (2013) Insights into early Earth from Barberton komatiites: evidence from lithophile isotope and trace element systematics. Geochim Cosmochim Acta 108:63–90

Radhakrishna BP (1957) Mode of occurrence of chromite at Byrapur, Mysore State, India. Mysore Geol Assoc Bull 12:13

Radhakrishna BP, Naqvi SM (1986) Precambrian continental crust of India and its evolution. J Geol 94:145–166

Roeder PL, Campbell IH, Jamieson HE (1979) A re-evaluation of the olivine-spinel geothermometer. Contrib Mineral Petrol 68:325–334

Rollinson H (1995) The relationship between chromite chemistry and the tectonic setting of Archean ultramafic rocks. In: Tromps P (ed) Blenkinsop TG. Sub-Saharan Econ Geol Amsterdam, Balkema, pp 7–23

Rollinson H (2008) The geochemistry of mantle chromitites from the northern part of the Oman ophiolite: inferred parental melt compositions. Contrib Mineral Petrol 156:273–288

Sattari P, Brenan JM, Horn I, McDonough WF (2002) Experimental constraints on the sulfide silicate and chromite-silicate melt partitioning behavior of rhenium and platinum-group elements. Econ Geol 97:385–398

Scowen PAH, Roeder PL, Helz RT (1991) Reequilibration of chromite within Kilauea Iki lava lake, Hawaii. Contrib Mineral Petrol 107:8–20

Skinner BJ, Luce FD, Dill JA, Ellis DE, Hagan HA, Lewis DM, Odell DA, Sverjensky DA, Williams N (1976) Phase relations in the ternary portions of the system Pt–Pd–Fe–As–S. Econ Geol 71:1469–1475

Stone WE, Crocket JH, Fleet ME (1990) Partitioning of palladium, iridium, platinum, and gold between sulfide liquid and basalt melt at 1200°C. Geochim Cosmochim Acta 54:2341–2344

Stowe CW (1994) Compositions and tectonic settings of chromite deposits though time. Econ Geol 89:528–546

Sun SS, Nesbitt RW, McCulloch MT (1989) Geochemistry and petrogenesis of Archaean and early Proterozoic siliceous highmagnesian basalts. In: Crawford AJ (ed) Boninites and related rocks. Unwin and Hyman, London, pp 148–173

Swami Nath J, Ramakrishnan M (1981) Early Precambrian supracrustals of Southern Karnataka. Geol Surv India Mem 112:363

Toplis MJ, Corgne A (2002) An experimental study of element partitioning between magnetite, clinopyroxene and iron-bearing silicate liquids with particular emphasis on vanadium. Contrib Mineral Petrol 144:22–37

Whitney DL, Evans BW (2010) Abbreviations for names of rock-forming minerals. Am Mineral 95:185–187

Yao S, (1999) Chemical composition of chromites from ultramafic rocks: application to mineral exploration and petrogenesis. PhD thesis, Macquarie University, Sydney p 174